TABLE OF CONTENTS

LIST OF FIGURES AND TABLES

CHAPTER II

CHAPTER III

ACKNOWLEDGEMENTS

The text of Chapter II is, in full, a reprint of the article as it appears in W. Geng *et al.* 2003, "C. elegans Egg-laying Detection and Behavior Study Using Image Analysis," submitted to EURASIP Journal on Applied Signal and Image Processing January 2004. Megan A. Palm contributed the majority of the data appearing in the paper and was involved in testing the image analysis program used.

ABSTRACT OF THE THESIS

Analysis of *Caenorhabditis elegans* behavior using an automated behavioral phenotype quantification system

by

Megan A. Palm

Master of Science in Biology

University of California, San Diego, 2005

Professor William R. Schafer, Chair

This thesis presents work done to improve and test an automated behavioral phenotype quantification system for use in the study of *Caenorhabditis elegans*. First, we present an algorithm developed for automatic egg-laying detection. Egg-laying is a behavior often studied in *C. elegans*, and when studying *C. elegans* egg-laying behavior using image analysis, it is important to be able to distinguish true egg-laying events from false positives. The ability to determine which parameters change before, during, and following an egg-laying event is also important, and is described in this thesis. The automated behavioral phenotype quantification system was then used to examine a *C. elegans* mutant involved in nicotinic acetylcholine receptor regulation. This mutant was previously characterized as having wild type behavior, but use of the automated behavioral phenotype quantification system allowed the determination that the mutant has a phenotype with subtle differences from wild type behavior. Through these studies, a greater insight into *C. elegans* behavior has been achieved.

CHAPTER I INTRODUCTION

The ability to obtain objective observations of behavior has long been a problem of interest in biology. With the advent of complete genome sequencing of model organisms such as the nematode *Caenorhabditis elegans*, it is now possible to determine the precise mutation carried by an animal and to correlate the mutation with a behavioral defect. Although the small size of *C. elegans* presents a difficulty when examining subtle phenotypes, advances in machine vision have now made it possible to utilize computers to classify behavioral patterns with far greater sensitivity than the human eye.

C. elegans is a relatively simple organism that nonetheless contains a great deal of versatility. It is capable of responding to diverse external stimuli, such as the presence of food, pharmacological treatments, the presence of other animals, temperature, ionic gradients, and touch stimuli. It is an attractive model organism for several reasons: 1) it has a short life cycle of approximately three days, 2) it is easily cultivated in the laboratory, 3) the majority of animals are self-fertilizing hermaphrodites, although males do occur, 4) it has a simple, if small, body structure without any appendages, and 5) its genome has been completely sequenced.

While *C. elegans* is an attractive model organism in many respects, its small size often makes direct behavioral observations problematic. Behavioral observations of *C. elegans* may be difficult, strenuous, or even impossible to quantitate when the parameter of interest, such as the angle of body bending, is changed by only a few micrometers. There is also the factor of human error. One observer may score a

phenotype in a different manner than another. However, with the assistance of computers, it is now possible to make direct, quantitative, and consistent observations of *C. elegans* with a minimum of effort.

Features that have been used in phenotypic characterizations of *C. elegans* include size, distance traveled, characteristics of body bending, reversal distance, and egg-laying behavioral patterns. Egg-laying in particular is an important feature of worm behavior as it may be used to study neuronal signal transduction. In the past, egg-laying in *C. elegans* was examined using video recordings and lengthy human analysis (Hardaker *et al.* 2001). Automated detection of egg-laying events allows for more precision in determining small yet significant changes in behavior as well as having the added benefit of being far less time-consuming.

Automated behavioral phenotype quantification allows researchers to quantitate behavioral observations and to examine changes in behavior which may be unobservable to the unaided eye. In worms with a previously characterized phenotype, such as uncoordinated, automated behavioral phenotype quantification allows the determination of which parameters contribute to the degree of uncoordination, which differs between worms of different genotypes. Combined with genetic analysis, this information may give certain insights into the link between a particular gene and its overall function in the organism. Automated behavioral phenotype quantification may also aid in determining differences among mutant worms that were previously characterized as pseudo-wild type.

Nicotinic acetylcholine receptors (nAchR's) are found in the muscles of *C. elegans*, and have been implicated in a wide variety of behaviors, ranging from

feeding (pharyngeal pumping) to locomotion (body muscle contraction) to mating (male spicule protraction). The role of one particular nAchR, the levamisole receptor, has been of great interest due to its involvement in egg-laying and locomotion behaviors. The levamisole receptor is a nicotinic receptor found in both the body and vulval muscles, named for its response to the antihelminthic drug levamisole. There are several levamisole-resistant *C. elegans* mutants that exhibit varying degrees of resistance to levamisole and other cholinergic agonists such as nicotine, as well as displaying locomotion behaviors ranging from severely uncoordinated to wild type.

The gene *lev-9* was previously characterized as a weak levamisole resistance gene with unknown molecular identity (Lewis *et al.* 1980b). *lev-9* mutants have been described in the literature as being pseudo-wild type in behavior (Lewis *et al.* 1980a). In order to test whether the automated behavioral phenotype quantification system could discover any differences among these *lev-9* mutants, mutant worms from each of the three known alleles of *lev-9* were tracked, as well as worms with mutations in genes related to *lev-9* and in genes implicated in muscular disorders. Although behavioral differences among the three alleles of *lev-9* may be undistinguishable to the unaided observer, data analysis from automated behavioral phenotype quantification provides a method for distinguishing the differences among the three alleles of *lev-9* as well as their differences from wild-type worms.

This thesis documents work aimed at developing an automated tracking and image analysis system for use in behavioral studies of *C. elegans*. Briefly, we present a method that automatically detects egg-laying behavior. An automated behavioral phenotype quantification and image analysis system was then used to examine worms

previously characterized as pseudo-wild type in behavior. Using this method, subtle yet distinct differences in locomotion behavior were observable between wild type and *lev-9* mutants.

CHAPTER II: *C. ELEGANS* EGG-LAYING DETECTION AND BEHAVIOR STUDY USING IMAGE ANALYSIS

ABSTRACT

Egg-laying is an important phase of the life cycle of the nematode *Caenorhabditis elegans (C. elegans)*. Previous studies examined egg-laying events manually. This paper presents a method for automatic detection of egg-laying onset using deformable template matching and other morphological image analysis techniques. Some behavioral changes surrounding egg-laying events are also studied. The results demonstrate that the computer vision tools and algorithm developed here can be effectively used to study *C. elegans* egg-laying behaviors. The algorithm developed is an essential part of a machine vision system for *C. elegans* tracking and behavioral analysis.

INTRODUCTION

The nematode *C. elegans* is widely used for genetic studies of development, cell biology, and gene regulation. In particular, because of its facile genetics, well-described nervous system, and complete genome sequence, it is particularly well suited to analysis of the molecular and cellular basis of nervous system function and development. The ability to functionally map the influence of particular genes to specific behavioral phenotypes makes it possible to use genetic analysis to functionally dissect the molecular mechanisms underlying poorly understood aspects of nervous system function such as addiction, learning and sensory perception. However, many genes with critical roles in neuronal function have effects on behavior that are difficult to describe precisely, or occur over time scales too long to be compatible with real-time scoring by a human observer. Therefore, to fully realize the potential of *C. elegans* for the genetic analysis of nervous system function, it is necessary to develop sophisticated methods for the rapid and consistent quantitation of mutant phenotypes, especially those related to behavior.

One of the most important behaviors for the analysis of neuronal signal transduction mechanisms is egg-laying. Egg-laying in *C. elegans* occurs when embryos are expelled from the uterus through the contraction of 16 vulval and uterine muscles (White *et al*., 1986). In the presence of abundant food, wild-type animals lay eggs in a specific temporal pattern: egg-laying events tend to be clustered in short bursts, or active phases, which are separated by longer inactive phases during which eggs are retained. This egg-laying pattern can be accurately modeled as a three-

parameter probabilistic process, in which animals fluctuate between discrete inactive, active, and egg-laying states (Waggoner *et al*., 1998). Egg-laying has also been shown to be coordinated with locomotion: specifically, animals undergo a transient increase in global speed immediately before each egg-laying event (Hardaker *et al*., 2001). Many neurotransmitters and neuronal signal transduction pathways have been shown to have specific effects on egg-laying behavior; thus it has become an important behavioral assay for the analysis of many neurobiological problems in *C. elegans*.

Computer vision tools (Baek *et al.*, 2002, Geng *et al.,* 2003, Geng *et al.,* 2004) have been used successfully in recording, tracking, defining, and classifying *C. elegans* morphology and locomotion behaviors. Because egg-laying is infrequent, it is well suited for analysis by automated imaging methods. In previous egg-laying studies (Hardaker *et al.,* 2001, Waggoner *et al.,* 2000, Zhou *et al.,* 1998), individual worm movements were videotaped and the centroid location and time information were saved at 1s intervals during recording. The entire videos were later played back and each video frame was examined by expert observers to look for egg and egg onset frames. In this paper, we present an algorithm that can identify eggs and egg onsets automatically. In addition, by combining this information with the features (locomotion, morphology, behavior, shape) extracted using our previously developed computer vision methods, we are able to uncover relationships between egg-laying events and other characteristics.

2. IMAGE ACQUISITION AND SEGMENTATION

2.1 Acquisition of the Video Images

Routine culturing of *C. elegans* was performed as described (Brenner 1974). All worms analyzed in these experiments were young adults; fourth-stage larvae were picked the evening before the experiment and tracked the following morning after cultivation at 22°. All animals used in this study were from the wild-type Bristol (N2) strain.

C. elegans locomotion was tracked with a stereomicroscope mounted with a CCD video camera (Baek *et al.,* 2002, Geng *et al.,* 2003, Geng *et al.,* 2004). The video camera used only a single eyepiece, so did not have stereo data; the system is equivalent to a conventional bright field microscope. A computer-controlled tracker was used to maintain the worms in the center of the optical field of the microscope during observation. To record the locomotion of an animal, an image frame of the animal was snapped every 0.5 second for at least five minutes (20 minutes or more in the longer recordings). Among those image pixels with values less than or equal to the average value minus three times the standard deviation, the largest connected component was found. The image was then trimmed to the smallest axis-aligned rectangle that contained this component, and saved as eight-bit grayscale data. The dimensions of each image and the coordinates of the upper left corner of the bounding box surrounding the image were also saved simultaneously as the references for the location of an animal in the tracker field at the corresponding time point when the images are snapped. The microscope was fixed to its largest magnification (50 X)

during operation. Depending on the type and the posture of a worm, the number of pixels per trimmed image frame varied. The number of pixels per millimeter was fixed at 312.5 pixel/mm for all worms.

2.2. Segmentation and tracking of the Worm Body

The segmentation process is presented in (Geng *et al.* 2004). Briefly, an adaptive local thresholding algorithm with a 5x5 moving window was used followed by a morphological closing operator (binary dilations followed by erosions). A corresponding reference binary image was also generated by filling the holes inside a worm body based on image content information. The difference between these two binary images provided a good indication of which image areas are worm body and which are background.

Following binarization, a morphological skeleton was obtained by applying a skeletonizing algorithm. Redundant pixels on the skeleton were eliminated by thinning. To avoid branches on the ends of skeletons, the skeleton was first shrunk from all its end points simultaneously until only two end points were left. These two end points represent the longest end-to-end path on the skeleton. A clean skeleton can then be obtained by growing out these two remaining end points along the unpruned skeleton by repeating a dilation operation.

The tracking algorithm is presented in (Geng *et al*. 2004), and included automatic recognition of the head and tail for the worm inside each frame.

3. MODEL-BASED ATTACHED EGG DETECTION

3.1. Image Analysis

To find the possible egg locations and limit the search area for deformable template matching, we developed a series of morphological image analysis algorithms to limit our search area to around 2% of a typical region that a worm body covers. The search is greatly expedited and match accuracy is improved by effectively eliminating potential false alarms. The flowchart of attached egg detection is shown in Fig. 1-1. For each input video frame, the worm body is first segmented from the background and the skeleton (medial axis) is obtained by algorithms described in (Geng *et al.,* 2004). The laying of an egg changes the shape of the binarized worm body (Fig. 1-2), which can be captured by examining the width profile in the middle part of the worm body in the following way. For each pixel in the skeleton pixel list, a straight line traversing the worm body that passes through that skeleton pixel is calculated. 71 additional lines are also calculated at 5-degree intervals to cover a 360 degree radius. The worm body width at that skeleton pixel is the shortest of the 72 lines, which has the shortest distance traversing the binary image through the skeleton pixel. In the case where the abnormal width is caused by an attached egg, one of the two end point locations on the shortest-distance line is enclosed by that egg. By abnormal width, we mean a difference greater than 7.5 pixels/24 μm between median and peak width in the middle part of the body, indicating a potential egg event. Fig. 1-2A shows the frame immediately prior to an egg-laying event. Fig. 1-2B shows the egg-laying frame. The corresponding width profiles are shown in Fig. 1-2C and 1-2D

respectively. The solid curves show the width measured along the worm skeletons. The horizontal dotted lines in Fig. 1-2C and 1-2D show the median width for the middle part of the worm body. A second horizontal line in Fig. 1-2D shows the threshold (7.5 pixels above the median width value) that defines abnormal width. The width profile curves are normalized to 300 pixels for comparison. Since egg laying is a rare event, over 90% of the frames are quickly passed through and not subject to further analysis.

Since the abnormal width measure can not tell us which side the egg is on (which end point the egg encloses), we extract the boundary from both sides of the worm body and consider the side that has higher *k*-curvature values to be the egg side. This way, the search area is constrained to only one side of the worm body and half of the search area is effectively eliminated. The process starts with isolating the body area containing the abnormal width by cutting off the worm body area that is 25 pixels/80 μm before and after using the minimal-distance straight lines passing through the skeleton pixels. This cutoff area is 51 pixels/160 μm in medial axis and has four boundaries. Two of the boundaries are the straight cutoff lines, and the other two are the two sides of the worm body (Fig. 1-3B). A boundary following algorithm similar to (Sonka *et al.,* 1999) is then used to extract the two boundaries along the sides of the worm body (Fig. 1-3C). The *k*-curvature ($k = [3,7]$) [Jain 1995] of these two boundaries is calculated, and the boundary that has higher (for all 5 *k*-curvature measurements) values is designated as the egg side. If neither boundary has all 5

measurements higher, both sides are checked for eggs. The *k*-curvature is defined as

$$R = \left\{ \frac{1}{n-1} \sum_{i=1}^{n-1} \theta_i \right\},$$

where $\theta_i = \arctan \frac{y_{i+2} - y_{i+1}}{x_{i+2} - x_{i+1}} - \arctan \frac{y_{i+1} - y_i}{x_{i+1} - x_i}$,

and $(x_i, y_i), (x_{i+1}, y_{i+1})$ **…** are the locations of consecutive points that are *k* pixels apart along the worm side boundaries.

Once the location of the maximal peak is decided, the search region Ω can be obtained by region growing out of the egg side end point to enclose the egg center. A directional dilation algorithm such as (Borgefors 1986) can be used for this purpose. Here we once again take advantage of the worm skeleton. The directional dilation is achieved by applying two constraints in the dilation process: (1) dilation starts from the end point and should remain inside the binary worm body; (2) dilation remains outside skeleton area (dilated 4 times from skeleton) (Fig. 1-3D). The dilation process stops when more than 200 pixels are inside the region. The directional dilation forces the search area to be inside the worm body close to the side boundaries rather than close to the skeleton. The final search region Ω (Fig. 1-3E) typically contains between 200 and 250 pixels for each frame. In the case that both sides are checked, a total of 400 pixels is checked. Fig. 1-3 illustrates the process.

3.2. Deformable template matching

Deformable template matching models have been applied to a variety of image recognition and analysis applications with success (McInerney *et al.* 1996, Jain *et al.* 1996,1998, Escolano *et al.*, 1997, Fisker *et al.* 2000). They enjoy not only the flexibility of a parameterized model, but also can be explained in a Bayesian framework. Even though the attached eggs could be partially obscured by shadows and/or by the worm body, or partially laid, they share many common characteristics. They tend to have oval shapes, and are generally brighter in the middle and darker around the boundary. The eggs are more or less similar in size. These characteristics make them ideal for the elliptic deformable templates.

In an ideal case, the shape of the attached eggs can be modeled by an elliptic model such as the one shown in Fig. 1-4 with 7 parameters $v = (x, y, a, b, \theta, \rho 1, \rho 2)$, where (x, y) are the coordinates of the center, a and b are the semi axes and θ is the rotation angle. Together, these 5 parameters control the geometric shape and location of the inner ellipse that captures the bright center part of the egg. $\rho 1$ equals the ratio between the area of the middle band and the inner ellipse, $\rho 2$ equals the ratio between the area of the outer band and the middle ellipse. The middle band encloses the dark exterior part of the egg. The outer band covers part of the worm body and part of the background. By studying the homogeneity of the pixels enclosed, the outer band can be used to suppress noise and find the best location for the egg. For example, if (x, y) is mistakenly inside the worm body, then the outer band will have similar

brightness to the worm body (dark). If (x, y) is in the background area, the outer band has similar brightness to the background (light). Half worm body and half background inside the outer band indicate a perfect attached egg location. To reduce model complexity, we opt to use a simplified model (Fig. 1-5) that does not have the outer band, and use image analysis to restrain the search area. The outer band in Fig 1-4, is only used for deletion purposes when multiple eggs/peaks are detected. In these cases, the pixels inside the entire outer ellipse are deleted and the process is repeated to detect additional eggs. The outer band is also shown in Fig. 1-3, 1-7 and 1-8 to mark the location of the best-fit ellipse. There are 6 parameters characterizing the shape of the simplified elliptic model $v = (x, y, a, b, \theta, \rho)$.

From a Bayesian framework, we have $p(v \mid E) = \dfrac{p(v)p(E \mid v)}{p(E)}$, where E is the event that the image contains an egg, and $p(v \mid E)$ is the probability density function of parameter configuration given that an egg is present. There are many ways to define the likelihood function. We propose the following model:

$$p(E \mid v) = \frac{1}{z}\exp\{-(\alpha\mu_{in}(v) + \beta\mu_{out}(v))\} \qquad (1)$$

where $\mu_{in}(v)$ is the mean pixel value inside the inner ellipse, $\mu_{out}(v)$ is the mean pixel value in the band around the inner ellipse (Fig. 5), and α, β are weights to be selected to give a proper weight for inside and outside areas. For calculating the mean values, the pixel intensities are linearly rescaled to go from –1 to +1. z is a

normalization constant to ensure that $p(E \mid v)$ is a proper probability density of unit area.

The egg finding problem can then be modeled as finding the most likely parameter configuration v_{opt} given that there is an egg in the image. Using a maximum a posteriori (MAP) estimator,

$$v_{opt} = \arg\max_{v} p(v \mid E) = \arg\max_{v} \frac{p(v)p(E \mid v)}{p(E)} \qquad (2)$$

Since the egg can occur in any orientation and location in the search space, it is reasonable to assume a uniform prior. For simplicity, we also assume a and b are uniformly distributed in a narrow range. So Equation 2 is identical to

$$v_{opt} = \arg\max_{v} p(E \mid v) = \arg\max_{v} \frac{1}{z} \exp\{-(\alpha\mu_{in}(v) + \beta\mu_{out}(v))\} \qquad (3)$$

Furthermore, because z is a constant, Equation 3 is identical to

$$v_{opt} = \arg\max_{v} \{\alpha\mu_{in}(v) + \beta\mu_{out}(v)\} \qquad (4)$$

The optimal parameter configuration is the parameter *v* that maximizes the function

$$U(v) = \alpha\mu_{in}(v) + \beta\mu_{out}(v). \qquad (5)$$

We chose $\alpha = 0.5$, $\beta = -1$, and $\rho = 8$ by feeding a small set of training samples of egg and non-egg values of μ_{in}, μ_{out} into the Classification and Regression Tree (CART) algorithm (Breiman *et al*. 1984). The final model for locating eggs is as follows:

For a specified search space Ω in the image, find

$$v_{opt} = (x_{opt}, y_{opt}, a_{opt}, b_{opt}, \theta_{opt}) = \arg\max_{v} U(v) \quad (6)$$

where $U = 0.5u_{in}(v) - u_{out}(v)$. Notice $U \in [-1.5, 1.5]$.

For every pixel (x_c, y_c) inside the search region Ω, U is calculated for each configuration with a range ($a = [3.4, 3.6], b = [1.9, 2.1], \theta = [0, 180]$). If U_{opt} is greater than a threshold value t, the location (x_{opt}, y_{opt}) is marked as the egg location and an egg is declared found.

3.3. Experimental Results

The egg detection algorithm was tested on 1,600 5-minute video sequences from 16 different mutant types (100 videos for each type) and five 20-minute video sequences of wild type animals treated with serotonin, which causes an increase in egg laying. The data were collected over a 3-year period by different individuals. A laborious manual check found 9,000 frames containing 200 different eggs. These eggs cover a wide variety of recording conditions, mutant types, sizes, and shapes. 100,000 non-egg frames were randomly selected from the rest of the 800,000 frames as non-egg cases. By applying the above algorithm with the decision threshold t varying from –1.5 to 1.5, the performance result is shown as a ROC curve (Metz 1978) in Fig. 1-6 and Table 1-1. The True Positive fraction is over 98% when the False Positive fraction is 1%. Fig. 1-7 shows some examples of the locations and best-fit ellipses identified by the algorithm. Some failure examples are shown in Fig. 1-8.

4. EGG ONSET DETECTION AND BEHAVIOR STUDY

4.1. Egg onset detection

Egg detection algorithms can be readily incorporated into a broader scheme for egg event onset detection (identifying the frames in which the egg first appears). Fig. 1-8 shows one algorithm to accomplish it. The main functions of the egg onset detection routine are to use the single frame egg detection result for a sequence. First, we decide whether the current egg is a newly laid or a previously laid egg (worms sometimes crawl back to previous eggs). This is accomplished by maintaining a list of all existing locations of eggs. When the new location is not on the list, an egg onset event is detected. Secondly, there are occasions when multiple eggs are laid at the same time. Also, there are cases when multiple width abnormalities are detected for a single frame due to multiple newly laid and previous eggs that remain near the worm body. The egg onset detection routine runs the single frame egg detection routine repeatedly in the search regions after the detected egg area (outer ellipse in the template model) is removed from the image in each run. This way, clusters of eggs can be detected. The egg onset detection routine also runs the abnormal width detection routine repeatedly to find out new search regions to detect all the eggs attached to the worm body.

The onset detection algorithm was tested on 25 videos of 20-minute recordings (500 minutes, 60,000 total frames). These recordings include 5 serotonin videos previously used for the egg detection test and 20 new normal wild type videos. By setting the thresholds conservatively (t=0.5) and declaring an egg onset has occurred if

one or more new eggs is detected in three or more consecutive frames, our algorithm is able to pick up all 88 egg onsets in one pass through the videos. There are 131 false alarm onset frames for the entire data set of 60,000 frames. The false alarm onsets are easily eliminated by inspecting each onset frame visually. Among the 88 onsets detected, there are 6 onsets that are delayed from true onsets by 1, 2, 3, 4, 10, 18 frames respectively.

4.2. Behavior Study

Previous study (Hardaker *et al*. 2001) indicated significantly increasing locomotion activity prior to egg onset. We studied the behavior changes before and after 55 wild type egg onsets (a fresh 10-hour recording) detected by our onset detection algorithm. The behavioral characteristics can be summarized by extracting features proposed by the feature extraction system (Baek *et al*. 2001, Geng *et al*. 2003, Geng *et al*. 2004). For each feature, we looked for a significant difference in that feature before and after the onset frame by using the non-parametric rank sum test on paired data. For each of the 55 eggs, we paired the data from 40 seconds before the onset frame with data after the onset frame. The 253 features examined include 131 morphological features (thickness, fatness, MER, Angle Change Rate, etc), 75 speed features (min, max and average speed over 1,5,10,20,30, 40sec, etc), 35 texture features (head, tail, center brightness, etc) and 12 other behavioral features (rate of reversals, omega shape, looping, etc). Out of these 253 features, 14 were found to be significant at the .01 significance level as shown in Table 1-2. We also considered the possibility that some features may be significantly different both before and after egg

laying compared to the values for a worm that is not near an egg-laying time. So we also looked at the paired data where the values from 40 seconds before an egg-laying onset were paired with the values from an equal number of frames starting from a randomly selected non-egg frame, and similarly where the values from after an egg-laying onset were paired with the values from an equal number of frames starting from a randomly selected non-egg frame. There were 32 (Table 1-3) comparisons that were significant at the .01 significance level for before and 32 after respectively. We note that, by random chance alone, out of 253 comparisons, we would expect to see 2.5 features to show a significant difference at the .01 significance level.

Most of the features found to be significantly different were related to speed, confirming earlier results that were determined manually. In particular, we found that the global centroid movement, as well as the local movement of the tail and head, were all significantly larger before the onset compared to after (see Fig. 1-10). Previous results only considered global movement. Local head movement is often related to foraging behavior. We also found some differences in brightness parameters. Due to the multiplicity of comparisons being made, these remain to be verified when further data are collected.

5. CONCLUSION

We have presented a computer analysis method for attached egg detection and egg onset event detection. The testing results of egg detection on 100,000 frames and 200 eggs from a variety of mutant types and recording conditions illustrate the

effectiveness of our proposed algorithm. The behavior study of egg onsets confirms the result from previous studies and shows promise for new findings.

The algorithm proposed is flexible to suit different needs. First, the abnormal width criteria (currently 7.5 pixels/24 μm) can be adjusted accordingly if prior knowledge of certain egg size and shape for a particular mutant is present, or the purpose is to obtain a rough idea of whether an egg is present. Secondly, the same applies to the decision criterion t according to the expectation of the false positive and false negative rate. Third, the current algorithm was applied on videos with frame rate of 2 Hz. The same algorithms can be applied to videos that have different frame rates. With increased frame rates, we anticipate an improved detection result.

With more accurate and complex computer vision systems (Baek *et al*. 2002, Geng *et al*. 2003, Geng *et al*. 2004) being developed, we anticipate that many more behavior features will be discovered. Therefore, we will be able to combine the automatic egg onset detection and behavior studies together and explore the temporal correlation between egg-laying and other behavioral characteristics more effectively. Moreover, the ability to automatically detect egg-laying events will make it possible to use these correlations between other behaviors and egg-laying, which previously could only be assayed through time-consuming human analysis of videotapes (Hardaker *et al*., 2001), as automatically-evaluated features for use in phenotype classification and clustering studies (Geng *et al*., 2003).

More generally, egg-laying has historically been an extremely useful assay for genetic analysis of diverse aspects of neuromuscular function. For example, egg-laying has provided a behavioral measure for the activity of the Go/Gq signaling network in neurons and muscle cells (Bastiani *et al.*, 2003) and for neuromodulation by serotonin, acetylcholine, and neuropeptides (Trent *et al.*, 1983; Weinshenker, *et al.*, 1999; Waggoner *et al.*, 2000). The egg-laying assays typically used in genetic studies are generally indirect measures of overall egg-laying rate, and consequently allow limited inference about the functions of specific mutant genes in the behavior. Quantitative assays of the temporal pattern of egg-laying can in principle make it possible to distinguish effects on different egg-laying signal transduction pathways (Waggoner *et al.*, 1998; Waggoner *et al.*, 2000). The automated methods for egg detection described here should greatly facilitate these more detailed behavioral analyses.

ACKNOWLEDGEMENT

We thank the Caenorhabditis Genetics Center for strains, Zhaoyang Feng for development and maintenance of the tracking system, Marika Orlov and Dan Poole for data collection, and Clare Huang who helped verify the egg results. This work was supported by a grant from the National Institute on Drug Abuse.

Fig. 1 Flowchart of the egg detection process

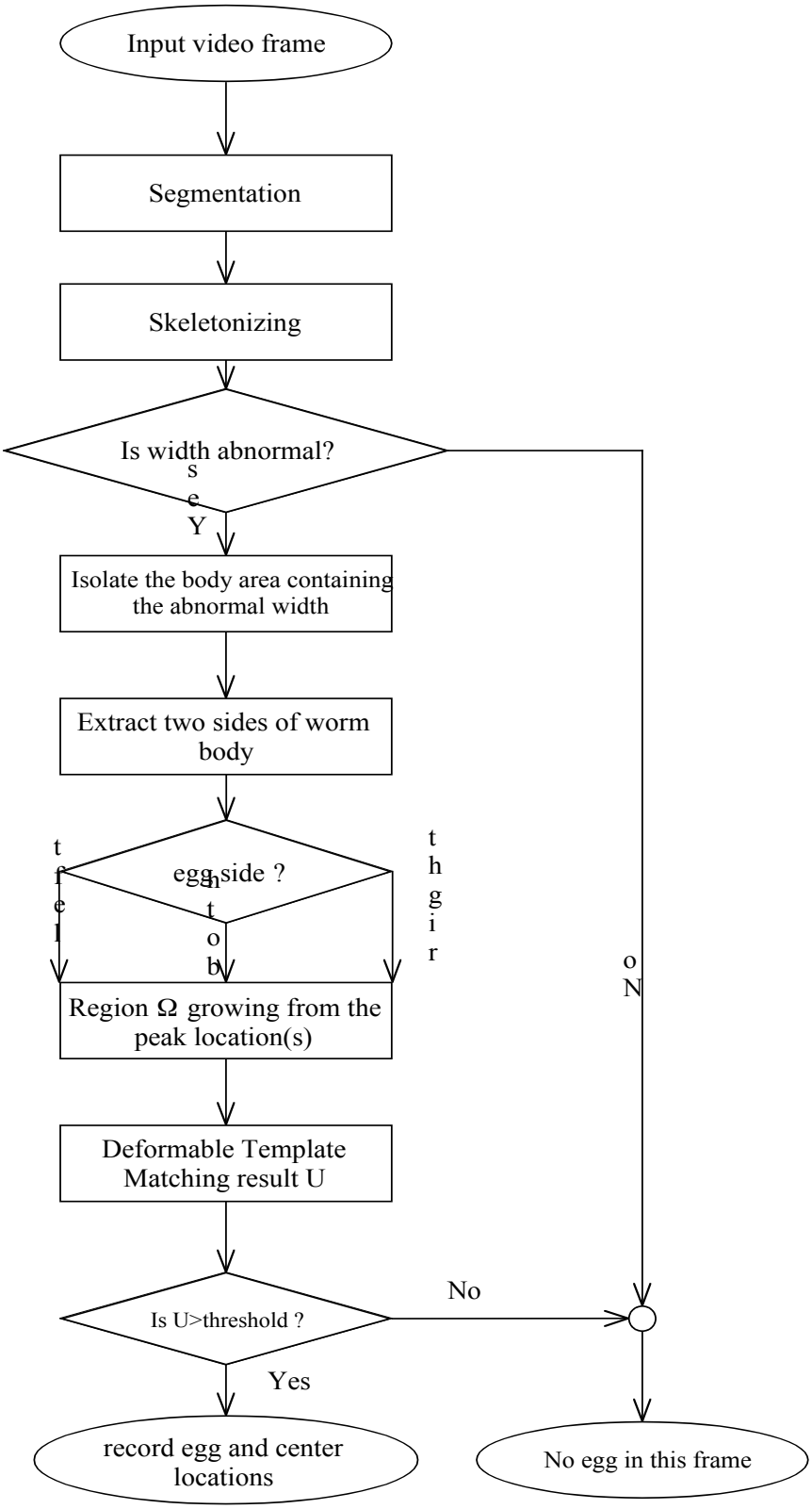

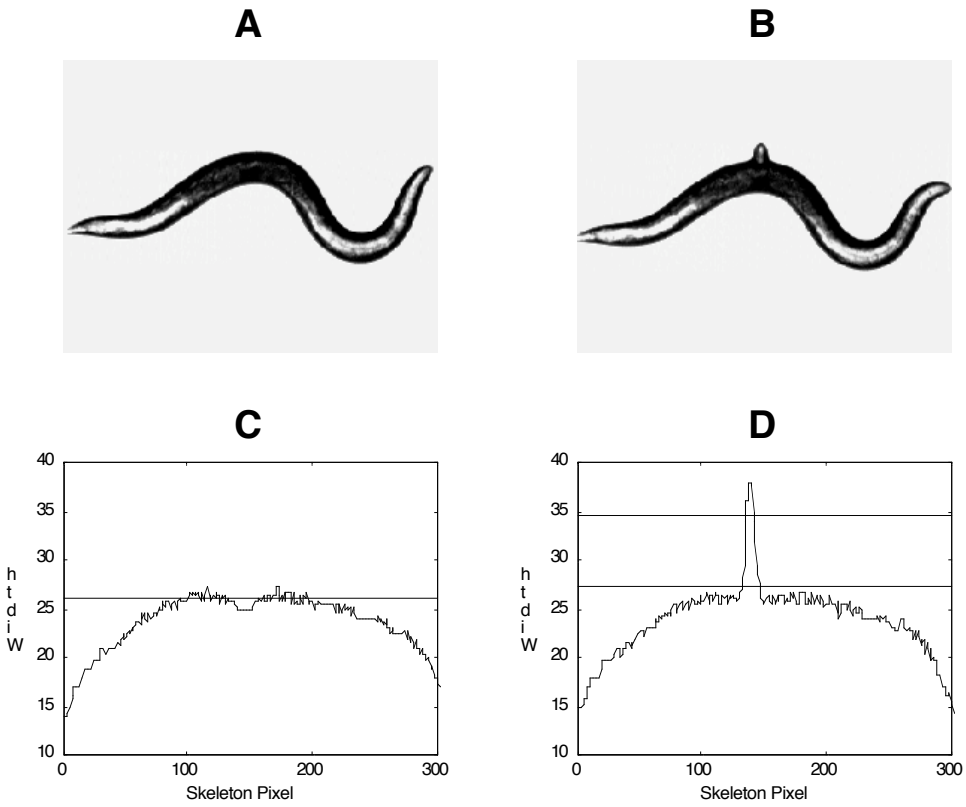

Fig. 2. Width profile change on egg onset. (A) Gray image right before egg onset. (B) Gray image right after egg onset. (C) Width profile of (A). The dotted line is the median value of the middle part of the width profile. (D) Width profile of (B). The lower dotted line is the median value of the middle part of the width profile. The upper dotted line is 7.5 pixels above the lower dotted line.

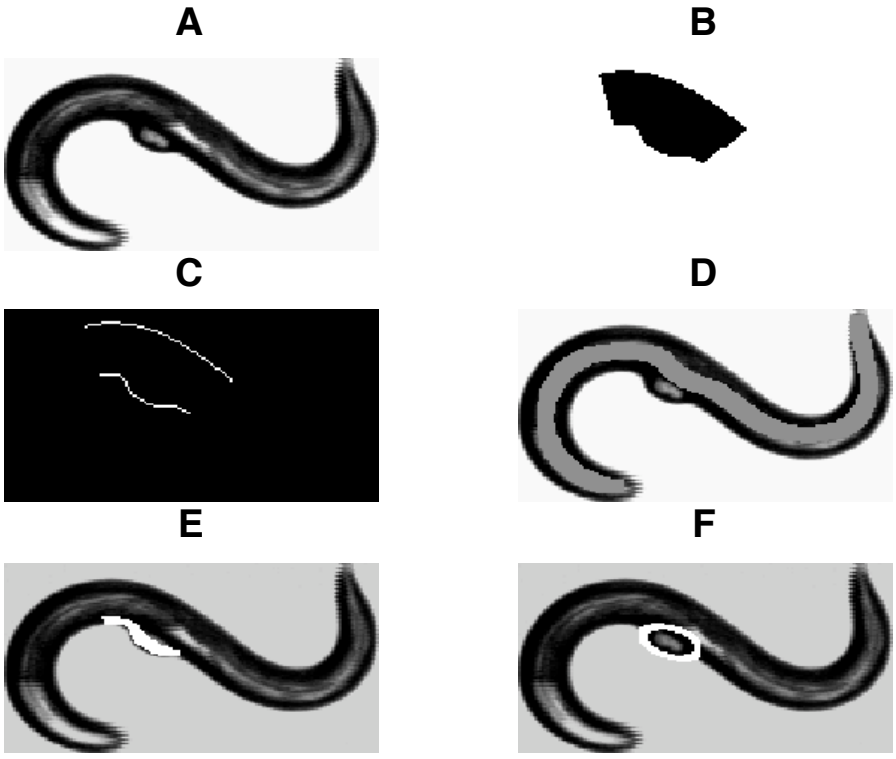

Fig. 3. Illustration of egg detection image analysis. (A) Gray scale image. (B) The cutoff portion containing egg. (C) Two boundaries. (D) The highlighted area (gray) shows dilating the skeleton four times. This area is not searched for eggs. (E) The highlighted area (white) shows final search region. (F) Best-fit ellipse.

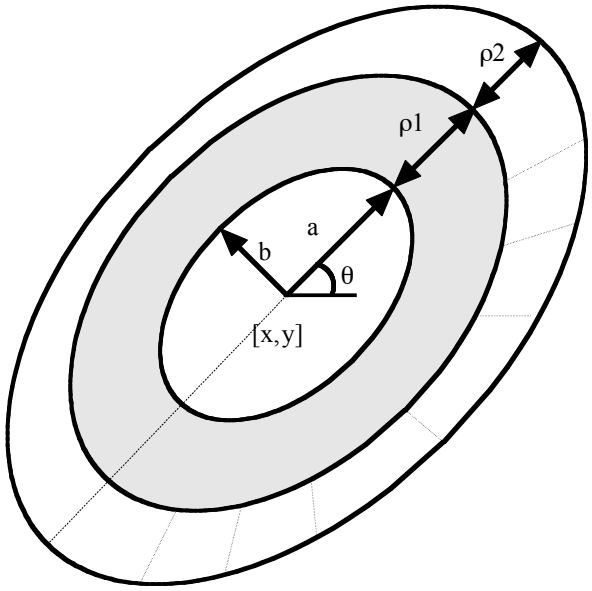

Fig. 4. Ellipse egg model.

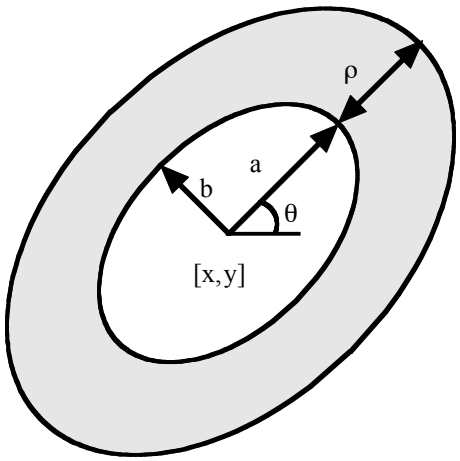

Fig. 5. Simplified ellipse egg model.

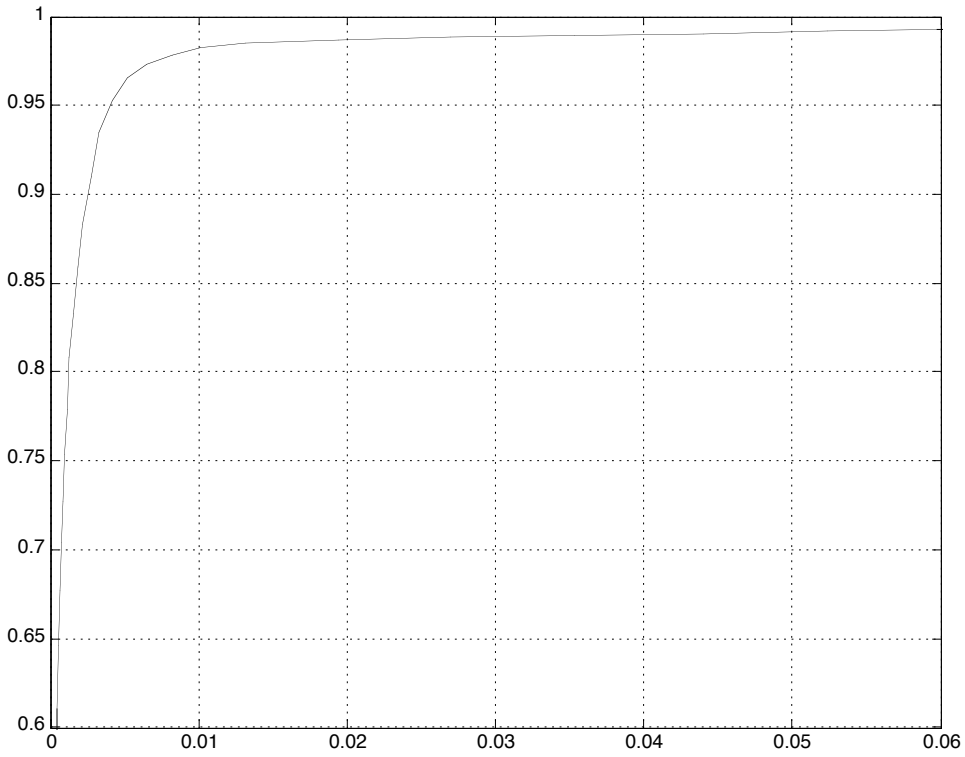

Fig. 6. A plot of the receiver operating characteristic (ROC) curve with threshold t varying from –1.5 to 1.5.

Rate of non-egg frames detected as egg (False positive)	Rate of egg frames detected as egg (True Positive)	Rate of egg frames detected as non-egg frames (False Negative)	Rate of non-egg frames detected as non-egg frames (True Negative)	Threshold t
0.0967	0.9985	0.0015	0.9033	0.35
0.0947	0.9983	0.0017	0.9053	0.36
0.0924	0.998	0.002	0.9076	0.37
0.0893	0.9977	0.0023	0.9106	0.38
0.0857	0.9972	0.0028	0.9143	0.39
0.0814	0.9964	0.0036	0.9186	0.4
0.0769	0.9961	0.0039	0.9231	0.41
0.072	0.9955	0.0045	0.928	0.42
0.0663	0.9946	0.0054	0.9337	0.43
0.0597	0.9927	0.0073	0.9403	0.44
0.0524	0.9915	0.0085	0.9476	0.45
0.044	0.9902	0.0098	0.956	0.46
0.0354	0.9893	0.0107	0.9646	0.47
0.027	0.9883	0.0117	0.973	0.48
0.0194	0.9865	0.0135	0.9806	0.49
0.0131	**0.9851**	**0.0149**	**0.9869**	**0.5**
0.0101	0.9826	0.0174	0.9899	0.51
0.0082	0.9785	0.0215	0.9918	0.52
0.0065	0.9729	0.0271	0.9935	0.53
0.0052	0.9658	0.0342	0.9948	0.54
0.0042	0.9531	0.0469	0.9959	0.55

Table 1: The false positive, true positive, false negative, and true negative values for part of the ROC curve. The boldface row is the final threshold used in the egg onset detection.

Features	Description
TLMV10MIN	Minimal tail movement in 5 seconds
TLMV10AVG	Average tail movement in 5 seconds
HDMV10AVG	Average head movement in 5 seconds
TLMVHFMIN	Minimal tail movement in 0.5 second
HDMV10MAX	Maximal head movement in 5 seconds
REVSALTIM	Total percentage of time worm stays in reversal position
HTBRDMIN	Minimal head and tail area brightness difference
HTBRRMIN	Minimal head/tail brightness
BANGCRMIN	Minimal whole body area angle change rate
LNWDRMAX	Maximal length to width ratio of the bounding box
BANGCRAVG	Average whole body area angle change rate
TLAMPMAX	Maximal amplitude in the tail area
AMPMAX	Maximal amplitude of worm skeleton wave
HDTLANMIN	Minimal head to tail angle

Table 2: The features changed significantly 40-second before and after egg onsets.

Features	Description	Features	Description
HDMVHFMIN	Min head movt. in _ sec	WHRATMIN	Min width-to-height ratio of MER
HDMVHFMAX	Max head movt. in _ sec	MAJORMIN	Min length of major axis
HDMVHFAVG	Average head movt. in _ sec	AMPRMIN	Min amplitude ratio
HDMV10MAX	Max head movt. in 5 sec	AMPRMAX	Max amplitude ratio
HDMV10AVG	Avg. head movt. in 5 sec	ANCHRMAX	Max angle change rate
HDMV20MAX	Max head movt. in 10 sec	ANCHSMAX	Max angle change standard deviation
HDMV20AVG	Avg. head movt. in 10 sec	CANGCRMIN	Min angle change rate in middle sect.
TLMV10MAX	Min tail movt. in 5 sec	CANGCRMAX	Max angle change rate in middle sect.
TLMV10AVG	Avg. tail movt. in 5 sec	CANGCRAVG	Avg. angle change rate in middle sect.
TLMV20AVG	Avg. tail movt. in 10 sec	BANGCRMAX	Max body angle change rate
RV20MAX	Max reversals in 10 sec	HDAMPMIN	Min amplitude in head
RV20AVG	Avg. reversals in 10 sec	TLAMPMAX	Max amplitude in tail
TOTRV	Total reversals in 5 minutes	CNTAMPMIN	Min amplitude in center
REVSALTIM	Total percentage of time worm stays in reversal position	AVGAMPMIN	Avg. amplitude
TAILBRMIN	Min tail brightness	HDTLANMAX	Max. head to tail angle
TAILBRAVG	Avg. tail brightness	TLANGMAX	Max. head angle change rate

Table 3: The features which changed significantly between 40 seconds before an egg onset and 40 seconds starting from a randomly selected non-egg frame.

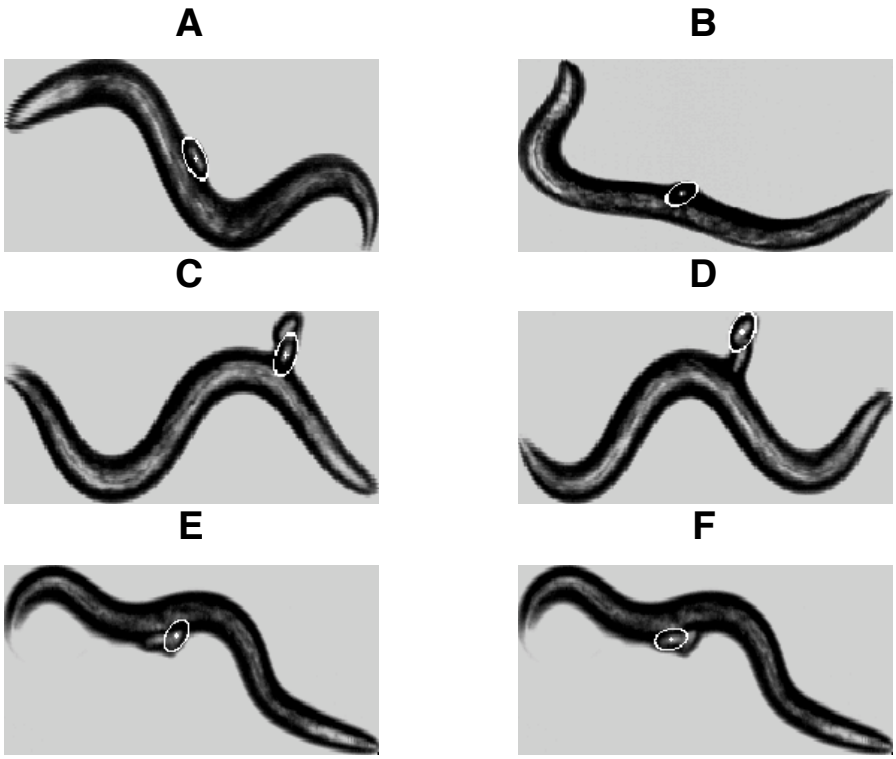

Fig. 7. Some best-fit results of deformable template matching. Some figures are rotated for plotting. (A) A fully laid egg in perfect condition. (B) A half laid egg. (C-D) Stacked eggs, identified by repeating the search. (E-F) Two eggs laid together with close distance.

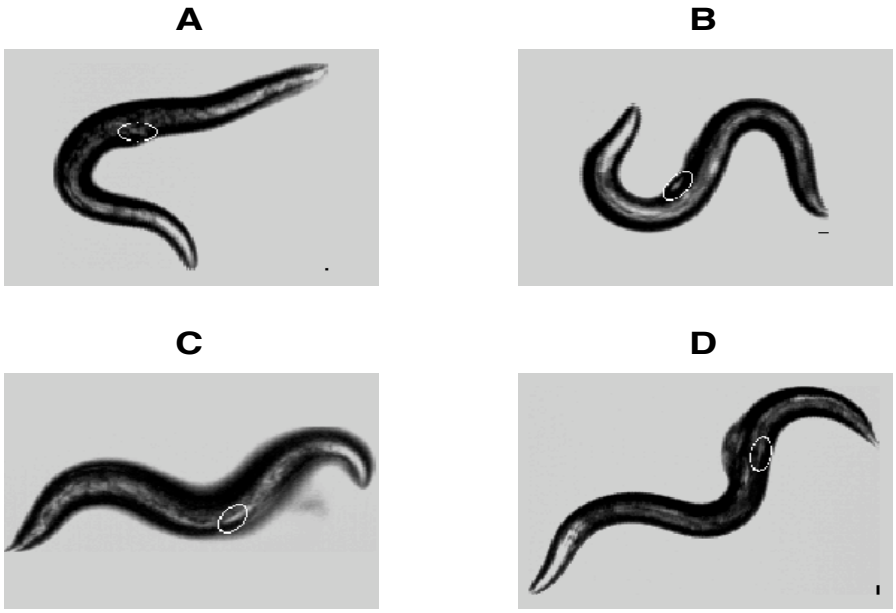

Fig. 8. Some non-egg frames that are identified as eggs.

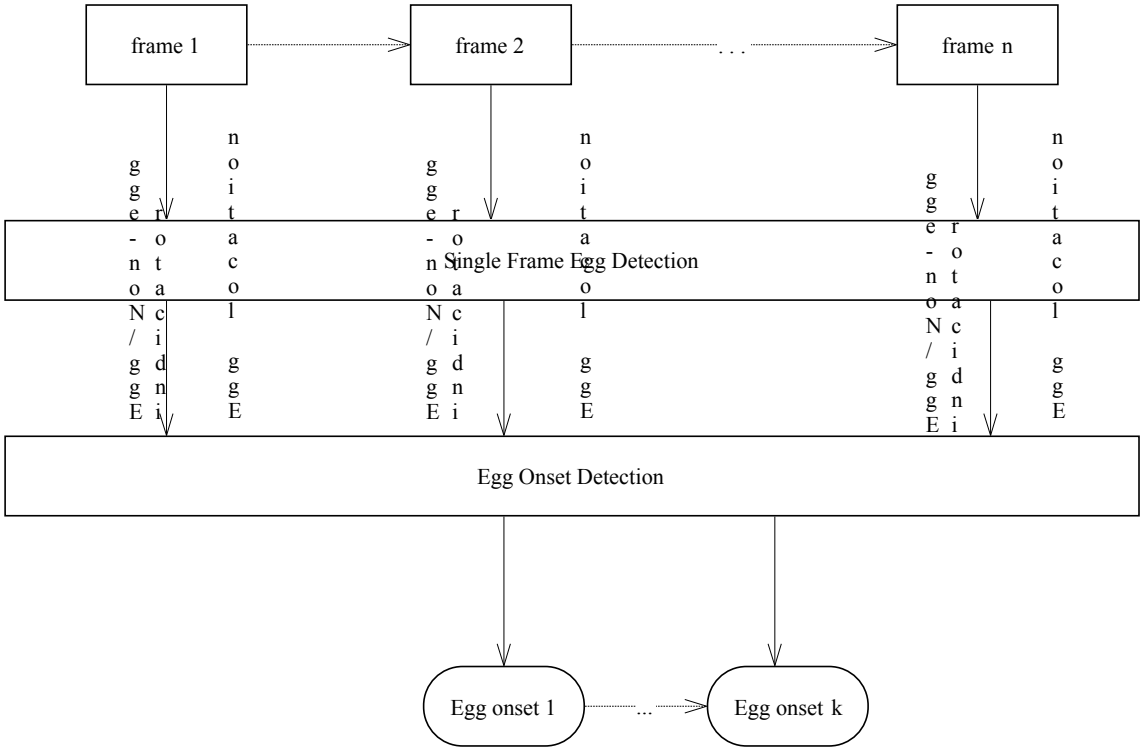

Fig. 9. Flowchart of egg event onset detection

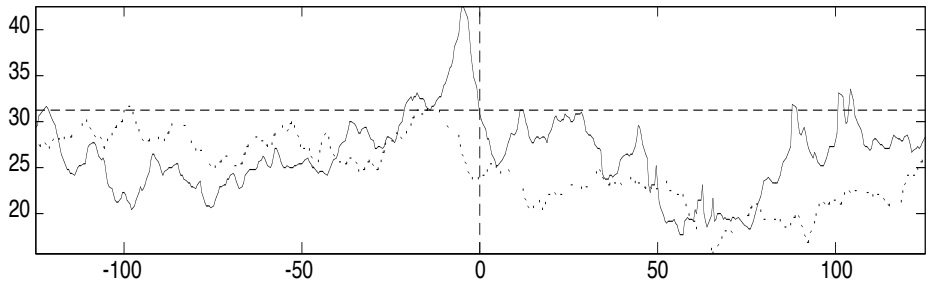

Fig. 10. Velocity change 125s before and after egg onset. The velocity is a moving average of 10s interval. (A) Centroid velocity. (B) Head velocity. (C) Tail velocity.

CHAPTER III: BEHAVIORAL STUDIES OF *CAENORHABDITIS ELEGANS* NICOTINIC ACETYLCHOLINE RECEPTOR MUTANTS USING IMAGE ANALYSIS

INTRODUCTION

The study of muscle contraction at the cellular level has long been a problem of interest in biology. In particular, the role of nicotinic acetylcholine receptors (nAChR's) in muscle contraction has been well-studied. nAchR's are heteropentameric ligand-gated ion channels found at the neuromuscular junction, where they mediate rapid excitation leading to muscle contraction. In the body muscles of *C. elegans*, there are two distinct nicotinic receptor subtypes known to mediate excitation of the body muscles (Richmond and Jorgenson 1999). One of these is activated by levamisole, a nematode specific antihelminthic drug, and is therefore known as the levamisole receptor. Wild type worms become paralyzed when exposed to levamisole. During a screen for levamisole-resistant *C. elegans* mutants, three alleles of the gene *lev-9* were identified (Lewis *et al.* 1980a). It is hypothesized that *lev-9* acts indirectly to regulate the levamisole receptor, but its exact function remains unknown (Lewis *et al*. 1987; Lewis *et al*. 1980a).

lev-9 mutants were previously described as weakly resistant to levamisole but pseudo-wild type in behavior (Lewis *et al.* 1980b). The three known alleles of *lev-9* have varying degrees of resistance to levamisole, which led to the question of whether or not the three mutants had different behavioral patterns both from each other and from wild type worms. To answer this question, the automated behavioral phenotype quantification system described in Geng *et al.* 2003 was used to compare the behavior

of *lev-9* mutants to the behavior of wild type worms, as well as to other strains with mutations in muscle-related genes.

RESULTS

In order to determine whether there was a true difference between the behaviors of the three alleles of *lev-9* and wild type worms, the automated behavioral phenotype quantification system described in Geng *et al.* 2003 was used to analyze *lev-9(x16)*, *lev-9(x62)*, *lev-9(x66)*, as well as wild type worms. In addition, the following mutant worms were tracked: *unc-29(x29)*, *lev-10(x17)*, *lev-1(x427)*, *dys-1(cx18)*, *dyb-1(ls292)*, and *H22K11.4(tm1232)X*. *unc-29* and *lev-1* are both known to encode non-_ receptor subunits of the levamisole receptor (Lewis *et al*. 1997). *lev-10* encodes a protein required for localization of acetylcholine receptors (Gally *et al.* 2004). The other three strains tracked carry mutations in genes involved in muscle organization.

dys-1 encodes an orthologue of human dystrophin (Gieseler *et al.* 1999), a protein found at the subsarcolemmal region in skeletal muscle that links the intracellular cytoskeleton to the extracellular matrix, and has also been implicated in organization of postsynaptic membrane and AChRs (Sadoulet-Puccio and Kunkel, 1996). *dyb-1* encodes a homologue of mammalian _-dystrobrevin (Bessou *et al.* 1998), a protein that binds directly to dystrophin and the sarcoglycan complex (Compton *et al.* 2005). *H22K11.4* encodes a homologue of mammalian _-sarcoglycan, a component of the sarcoglycan complex, which is intimately associated with dystrophin and dystroglycan to form the dystrophin glycoprotein complex

(Ervasti and Campbell 1993). Using the automated tracking system, we observed distinct differences between the behaviors of mutant worms of the three *lev-9* alleles and wild type worms.

Cluster Plot Analysis

Forty five-minute recordings were taken of individual adult hermaphrodites for each strain. For each recording, 152 features were measured that described body position and speed (Table 4). Using principle component analysis (PCA) and the methods described in Geng *et al.* 2003, a two-dimensional projection of all features was obtained (Figure 11). A classification tree is shown in Figure 12 that represents the features used in the clustering of all ten strains. Figure 13 contains bar graphs with the average value for the entire strain for the top three features in the classification tree. Interestingly, *lev-9(x16)* and *lev-9(x62)* clustered on the opposite side of the graph from wild type, indicating that those two strains have the most behavioral differences from wild type among the strains studied. Among the three alleles of *lev-9* previously characterized, *lev-9(x16)* has the strongest resistance to levamisole, while *lev-9(x62)* has intermediate resistance (Lewis *et al.* 1980a). Also of interest is the fact that *lev-9(x66)* clustered in the middle of the graph, reflecting its increased sensitivity to levamisole which resembles wild type response.

unc-29(x29), a mutant described as uncoordinated, clustered in the center between wild type and *lev-9(x16)*. This result was unexpected, given that *unc-29(x29)* is described as uncoordinated, while the mutants of *lev-9* are described as pseudo-wild type. To test whether *unc-29(x29)* was clustering in the correct region, data obtained

from recordings of mutant strains known to be severely uncoordinated were added to the cluster plot (Figure 14). Even after the addition of these mutants, the relationship between the representative centers of the original nine mutant strains and wild type remained unchanged, leading to the conclusion that the clustering is correct. *lev-9* mutants, though originally characterized as pseudo-wild type, have subtle yet distinct differences in behavior when compared to wild type.

Comparisons of wild type and *lev-9* worms

Once the cluster plot had been obtained, we were interested in identifying the specific features that had different values in wild type and *lev-9* worms. One feature of interest was the average distance traveled by each strain during set periods of time. Figures 15, 16, and 17 are graphs showing the net distance traveled by strain over three lengths of time: 0.5, 1 and 5 seconds, as measured by the features MVHLFAVG, MV1AVG, and MV5AVG. As the time intervals increased, a definite difference appeared between the distance traveled by *lev-9(x16)* animals and wild type animals. *lev-9(x16)* does not appear to travel as far as wild type worms over a period of five seconds, although when the distances traveled over 0.5 seconds are compared, *lev-9(x16)* does not appear travel a significantly smaller distance. This could indicate that *lev-9(x16)* is more prone to changing and reversing direction than wild type worms. *lev-9(x62)* and *lev-9(x66)* animals did not show significant changes in distance traveled at any of the three time points, although their average distance traveled fell below that of wild type animals.

Other parameters of interest include those that measure the body bending angles of the worms. These features are useful when examining phenotypes such as uncoordinated or loopy, and they also have great potential for measuring differences that are not easily identified by eye. Given that the net distance traveled by *lev-9(x16)* over a period of 5 seconds is less than the distance traveled by wild type, we were interested in determining if there was a change in *lev-9(x16)* body bending angles when compared with wild type body bending angles.

The features HDANGAVG, TLANGAVG, and CNTANGAVG were examined for differences between wild type and *lev-9(x16)* animals. HDANGAVG and TLANGAVG describe the average head and tail angle changing rate, respectively, and CNTANGAVG describes the average center angle changing rate. The areas of the worm body identified as the head region and tail region are each approximately 1/6 of the length of the total worm body (Geng *et al.* 2004). Interestingly, HDANGAVG and TLANGAVG did not show significant differences between wild type and *lev-9* worms (Figure 18), but when comparing the values of CNTANGAVG for wild type and the three *lev-9* mutants, a difference can be seen. For each of the three *lev-9* mutants, the average center angle changing rate is greater than that of wild type animals, with *lev-9(x66)* having the closest center angle changing rate to wild type, and *lev-9(x16)* having the greatest difference in rate.

DISCUSSION

Cluster Plot Analysis

Several observations may be made upon examination of the cluster plot in Figure 11. The representative centers of *lev-9(x16)* and *lev-9(x62)* are found in different regions than the representative center of wild type worms, leading to the conclusion that although these worms were previously characterized as pseudo wild type (Lewis *et al.* 1980b). These two alleles of *lev-9* also show stronger levamisole resistance than *lev-9(x66)*, a strain whose representative center was found to be between those of wild type and *lev-9(x16)*. The representative centers of *dyb-1(ls292)* and *dys-1(cx18)* are also close together, which is to be expected since those two strains contain mutations in related genes. The representative centers of *lev-1(x427)* and *lev-10(x17)* are in the same region as the centers of *lev-9(x16)* and *lev-9(x62)*, which is of interest given that *lev-1* encodes a non-_ receptor subunit of the levamisole receptor (Fleming *et al*. 1997) and *lev-10* encodes a protein required for localization of acetylcholine receptors (Gally *et al.* 2004).

Comparisons of wild type and *lev-9* worms

Two of the features that differed between *lev-9(x16)*, the mutant with the strongest levamisole resistance, and wild type were those that measured net distance traveled in five seconds (Figure 17) and the angle changing rate of the center of the worm (Figure 19). However, when comparing the distance traveled in 0.5 seconds and in one second, there was no significant difference between wild type and *lev-9(x16)* worms (Figures 15 and 16). This indicates that *lev-9(x16)* worms may reverse

and change direction far more often than wild type worms. This result could be confirmed by doing further studies comparing reversal distances and frequencies of *lev-9* mutants to those of wild type worms. The higher center angle changing rate observed in *lev-9(x16)* worms, as well as the other two *lev-9* mutants, is also an indication that *lev-9(x16)* worms change direction more frequently than wild type worms (Figure 19).

Automated behavioral phenotype quantification system

The automated behavioral phenotype quantification system used in this thesis has been previously used to examine mutants with widely differing behaviors (Geng *et al.* 2003). The work described in this thesis has demonstrated that even mutants with subtle phenotypes may demonstrate measurable differences in behavior from wild type worms. In the future, it may be possible to examine a mutant using this system, and then to examine the same mutant injected with a rescue construct to determine if the rescue was effective. Once the levamisole receptor is molecularly and genetically characterized, a comparison could be made of all levamisole-related mutants to determine their similarities and differences, regardless of whether or not the phenotype is subtle when observed by eye. Correlations may also be made between the drug resistance of a mutant and its behavior. While it is of definite use to researchers to be able to examine large differences in behavior, it is also important to have the ability to study mutants whose phenotypes are subtle, and the system described in this thesis may be used for those studies.

METHODS

Strains

Routine culturing of *C. elegans* was performed as described (Brenner 1974). The strains used are wild-type Bristol N2 strain, *lev-9(x16)*, *lev-9(x62)*, *lev-9(x66)*, H22K11.4*(tm1232)*, *dys-1(cx18)***,** *dyb-1(ls292)*, *unc-29(x29), lev-1(x427),* and *lev-10(x17)*.

Tracking Protocol

All worms analyzed in these experiments were young adults; fourth-stage larvae were picked approximately 16 hours before the experiment and tracked after cultivation at 22° C. Plates for tracking experiments were prepared fresh the day of the experiment; a single drop of a saturated LB culture of *E. coli* strain OP50 was spotted onto a fresh NGM agar plate and allowed to dry before use. A single adult worm was transferred to the freshly spotted plate and tracked immediately.

Image Data Collection and Feature Extraction

Worm locomotion and body position were monitored using a Zeiss Stemi 2000-C stereomicroscope mounted with a Cohu high-performance CCD video camera as described ((Baek *et al.* 2002). To record an animal's behavior, an image frame of the animal was snapped every 0.25 seconds for at least 5 minutes. For details of image preprocessing and feature extraction, see Geng *et al.* 2003 and Geng *et al.* 2004.

Table 4. List of features.

WORMNUM	worm index
AREAMIN	minimum worm body area
AREAMAX	maximum worm body area
AREAAVG	average worm body area
HGHTMIN	minimum height of the frame
HGHTMAX	maximum height of the frame
HGHTAVG	average height of the frame
WDTHMIN	minimum width of the frame
WDTHMAX	maximum width of the frame
WDTHAVG	average width of the frame
LNGTHMIN	minimum worm body length
LNGTHMAX	maximum worm body length
LNGTHAVG	average worm body length
WHRATMIN	minimum width/height ratio
WHRATMAX	maximum width/height ratio
WHRATAVG	average width/height ratio
MERFLMIN	minimum worm area to MER (minimum enclosing rectangle) area, (MER fill)
MERFLMAX	maximum worm area to MER (minimum enclosing rectangle) area, (MER fill)
MERFLAVG	average worm area to MER (minimum enclosing rectangle) area, (MER fill)
MAJORMIN	minimum length of best-fit ellipse's major axis
MAJORMAX	maximum length of best-fit ellipse's major axis
MAJORAVG	average length of best-fit ellipse's major axis
MINORMIN	minimum length of best-fit ellipse's minor axis
MINORMAX	maximum length of best-fit ellipse's minor axis
MINORAVG	average length of best-fit ellipse's minor axis
ECCTYMIN	minimum eccentricity of best-fit ellipse
ECCTYMAX	maximum eccentricity of best-fit ellipse
ECCTYAVG	average eccentricity of best-fit ellipse
MVHLFMIN	minimum distance moved in 0.5 second
MVHLFMAX	maximum distance moved in 0.5 second
MVHLFAVG	average distance moved in 0.5 second
MV1MIN	minimum distance moved in 1 second
MV1MAX	maximum distance moved in 1 second
MV1AVG	average distance moved in 1 second
MV5MIN	minimum distance moved in 5 second
MV5MAX	maximum distance moved in 5 second
MV5AVG	average distance moved in 5 second
HDTHKMIN	minimum head thickness
HDTHKMAX	maximum head thickness
HDTHKAVG	average head thickness
TLTHKMIN	minimum tail thickness
TLTHKMAX	maximum tail thickness
TLTHKAVG	average tail thickness
CNTHKMIN	minimum center thickness

Table 4 continued. List of features.

CNTHKMAX	maximum center thickness
CNTHKAVG	average center thickness
HDTLRMIN	minimum head's thick/length ratio
HDTLRMAX	maximum head's thick/length ratio
HDTLRAVG	average head's thick/length ratio
TLTLRMIN	minimum tail's thick/length ratio
TLTLRMAX	maximum tail's thick/length ratio
TLTLRAVG	average tail's thick/length ratio
CNTLRMIN	minimum center's thick/length ratio
CNTLRMAX	maximum center's thick/length ratio
CNTLRAVG	average center's thick/length ratio
HTTHRMIN	minimum head/tail thickness ratio
HTTHRMAX	maximum head/tail thickness ratio
HTTHRAVG	average head/tail thickness ratio
HCTHRMIN	minimum head/center thickness ratio
HCTHRMAX	maximum head/center thickness ratio
HCTHRAVG	average head/center thickness ratio
TCTHRMIN	minimum tail/center thickness ratio
TCTHRMAX	maximum tail/center thickness ratio
TCTHRAVG	average tail/center thickness ratio
AMPMIN	minimum amplitude of skeleton wave
AMPMAX	maximum amplitude of skeleton wave
AMPAVG	average amplitude of skeleton wave
AMPRMIN	minimum amplitude ratio of skeleton wave
AMPRMAX	maximum amplitude ratio of skeleton wave
AMPRAVG	average amplitude ratio of skeleton wave
ANCHRMIN	minimum angle changing rate of skeleton wave
ANCHRMAX	maximum angle changing rate of skeleton wave
ANCHRAVG	average angle changing rate of skeleton wave
ANCHSMIN	minimum angle changing rate (S.D.) of skeleton wave
ANCHSMAX	maximum angle changing rate (S.D.) of skeleton wave
ANCHSAVG	average angle changing rate (S.D.) of skeleton wave
LNMFRMIN	minimum ratio of worm length to MER fill
LNMFRMAX	maximum ratio of worm length to MER fill
LNMFRAVG	average ratio of worm length to MER fill
LNECRMIN	minimum ratio of length to eccentricity of best-fit ellipse
LNECRMAX	maximum ratio of length to eccentricity of best-fit ellipse
LNECRAVG	average ratio of length to eccentricity of best-fit ellipse
FATMIN	minimum fatness of worm (ratio worm area to length)
FATMAX	maximum fatness of worm (ratio worm area to length)
FATAVG	average fatness of worm (ratio worm area to length)
LNWDRMIN	minimum ratio of length to width

Table 4 continued. List of features.

LNWDRMAX	maximum ratio of length to width
LNWDRAVG	average ratio of length to width
CNTMVMAX	maximum moving distance of centroid
CNTMVAVG	average moving distance of centroid
HDWDMIN	minimum width of head
HDWDMAX	maximum width of head
HDWDAVG	average width of head
TLWDMIN	minimum width of tail
TLWDMAX	maximum width of tail
TLWDAVG	average width of tail
CNTWDMIN	minimum width of center
CNTWDMAX	maximum width of center
CNTWDAVG	average width of center
AVEWDMIN	minimum average of width
AVEWDMAX	maximum average of width
AVEWDAVG	average average of width
HTWRMIN	minimum head/tail width ratio
HTWRMAX	maximum head/tail width ratio
HTWRAVG	average head/tail width ratio
HDANGMIN	minimum head's angle changing rate
HDANGMAX	maximum head's angle changing rate
HDANGAVG	average head's angle changing rate
TLANGMIN	minimum tail's angle changing rate
TLANGMAX	maximum tail's angle changing rate
TLANGAVG	average tail's angle changing rate
CNTANMIN	minimum center's angle changing rate
CNTANMAX	maximum center's angle changing rate
CNTANAVG	average center's angle changing rate
AVEANMIN	minimum average angle changing rate
AVEANMAX	maximum average angle changing rate
AVEANAVG	average average angle changing rate
HAREAMIN	minimum area of head
HAREAMAX	maximum area of head
HAREAAVG	average area of head
TAREAMIN	minimum area of tail
TAREAMAX	maximum area of tail
TAREAAVG	average area of tail
CAREAMIN	minimum area of center
CAREAMAX	maximum area of center
CAREAAVG	average area of center
HDAMPMIN	minimum amplitude of head
HDAMPMAX	maximum amplitude of head
HDAMPAVG	average amplitude of head
TLAMPMIN	minimum amplitude of tail
TLAMPMAX	maximum amplitude of tail
TLAMPAVG	average amplitude of tail
CTAMPMIN	minimum amplitude of center

Table 4 continued. List of features.

CTAMPMAX	maximum amplitude of center
CTAMPAVG	average amplitude of center
AVAMPMIN	minimum average amplitude
AVAMPMAX	maximum average amplitude
AVAMPAVG	average average amplitude
HDCTDMIN	minimum distance of head to center
HDCTDMAX	maximum distance of head to center
HDCTDAVG	average distance of head to center
TLCTDMIN	minimum distance of tail to center
TLCTDMAX	maximum distance of tail to center
TLCTDAVG	average distance of tail to center
HTANGMIN	minimum angle between head-center and tail-center
HTANGMAX	maximum angle between head-center and tail-center
HTANGAVG	average angle between head-center and tail-center
HCANGMIN	minimum angle between head-center and horizontal line
HCANGMAX,	maximum angle between head-center and horizontal line
HCANGAVG,	average angle between head-center and horizontal line
TCANGMIN	minimum angle between tail-center and horizontal line
TCANGMAX	maximum angle between tail-center and horizontal line
TCANGAVG	average angle between tail-center and horizontal line

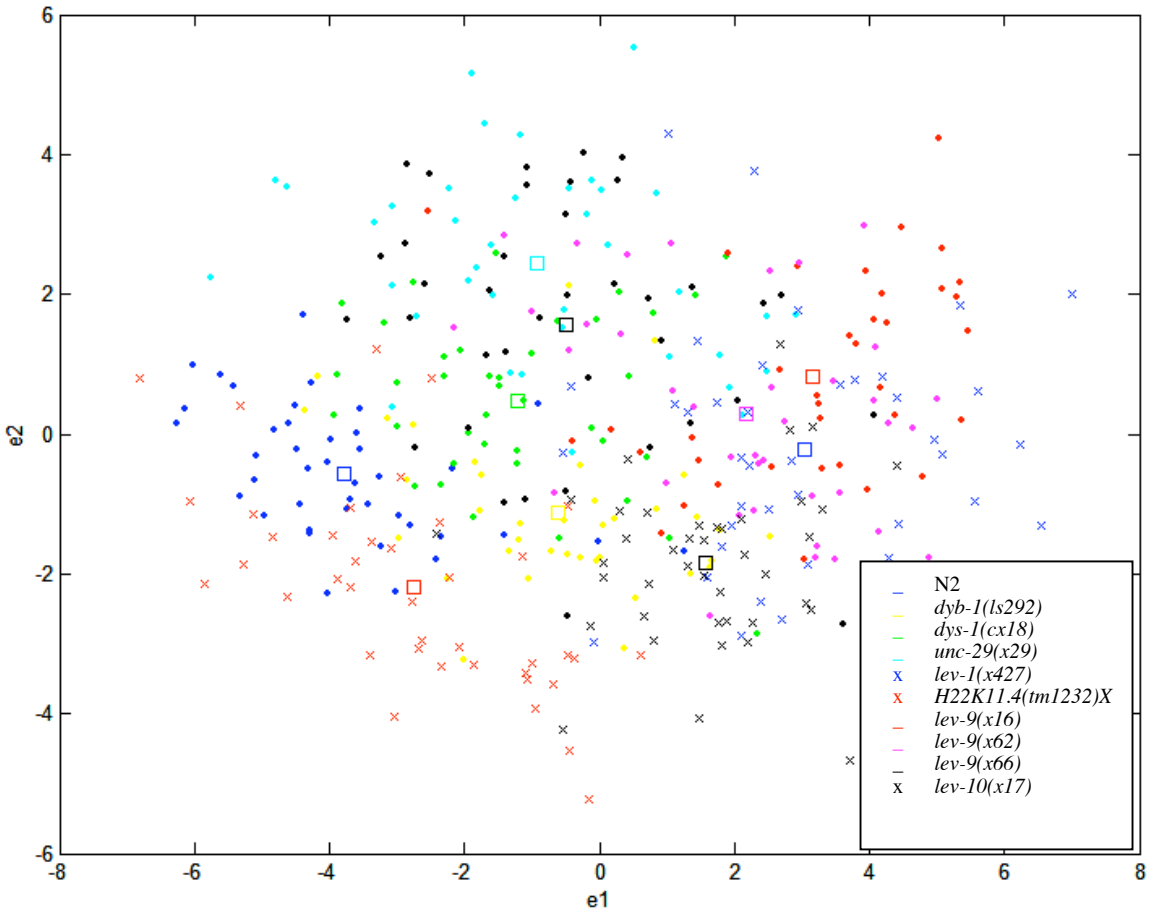

Figure 11. Distribution of behavioral data points in full feature space.
Each point on the graph represents one individual worm. Colored squares indicate the center of the data cloud as measured by Euclidean distance. The center is considered to be the prototype for each strain. N2 worms are clustered on the far left side of the graph, while *lev-9(x16)* and *lev-9(x62)* are clustered at the far right, with *lev-9(x66)* falling in the middle.

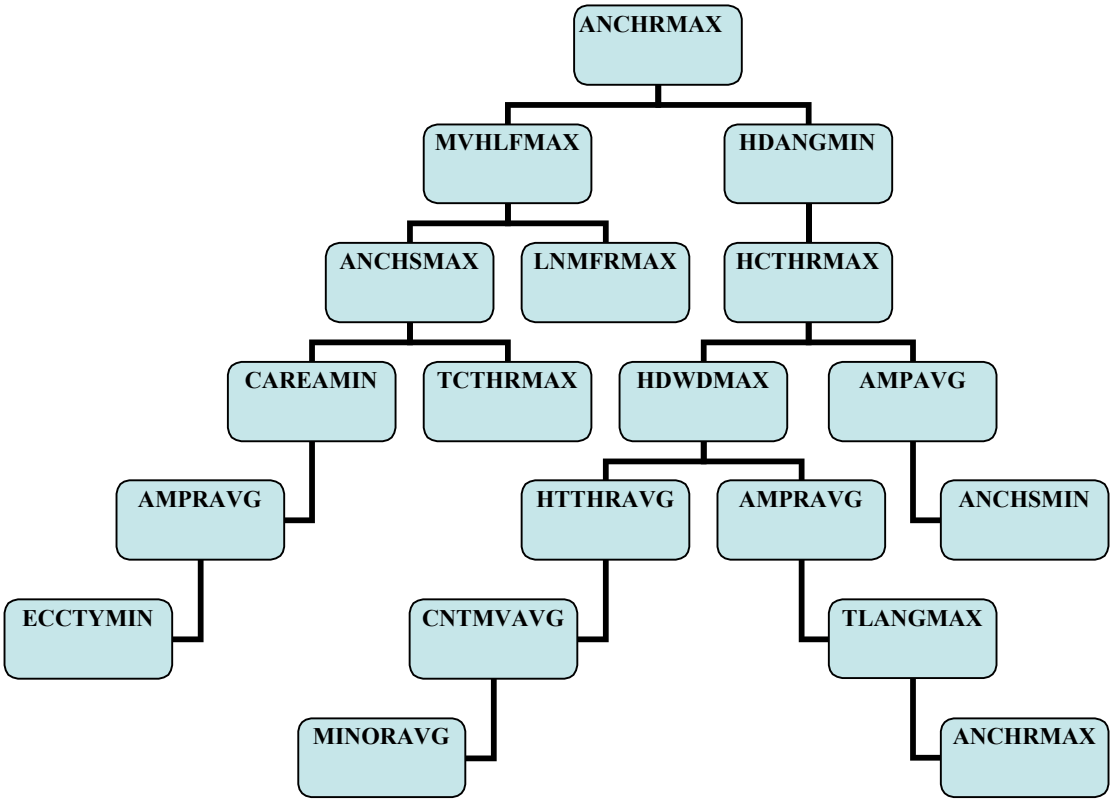

Figure 12 Classification tree. This classification tree lists the most important features used in differentiating between strains to create the cluster plot shown in Figure 3-1. Variables used were ANCHRMIN, minimum angle changing rate of skeleton wave; MVHLFMAX, maximum distance moved in 0.5 seconds; HDANGMIN, minimum head angle changing rate; ANCHSMAX, maximum angle changing rate standard deviation of the skeleton wave; LNMFRMAX, maximum ratio of worm length to minimum enclosing rectangle (MER) fill; HCTHRMAX, maximum head/center thickness ratio; CAREAMIN, minimum area of center; TCTHRMAX, maximum tail/center thickness ratio; HDWDMAX, maximum width of head; AMPAVG, average amplitude of skeleton wave; AMPRAVG, average amplitude ratio of skeleton wave; HTTHRAVG, average head/tail thickness ratio; ANCHSMIN, minimum angle changing rate standard deviation of the skeleton wave; ECCTYMIN, minimum eccentricity of best-fit ellipse; CNTMVAVG, average moving distance of centroid; TLANGMAX, maximum tail angle changing rate; MINORAVG, average length of best-fit ellipse's minor axis; ANCHRMAX, maximum angle changing rate of skeleton wave.

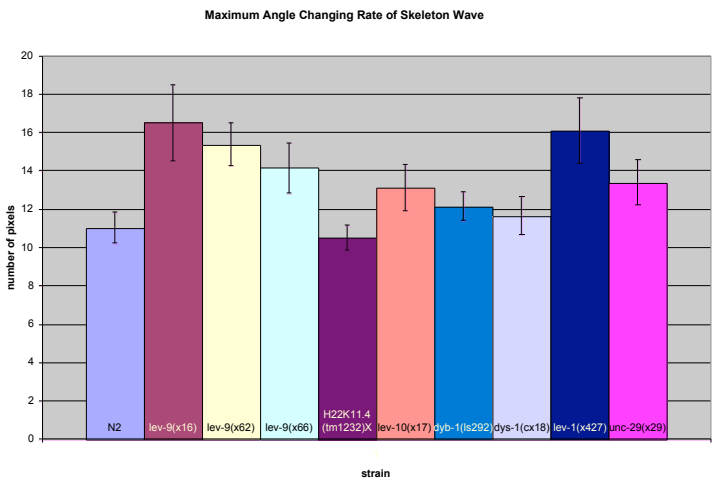

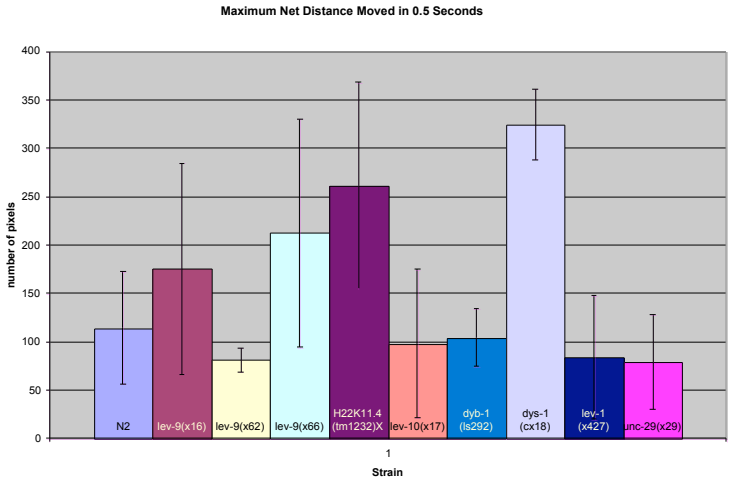

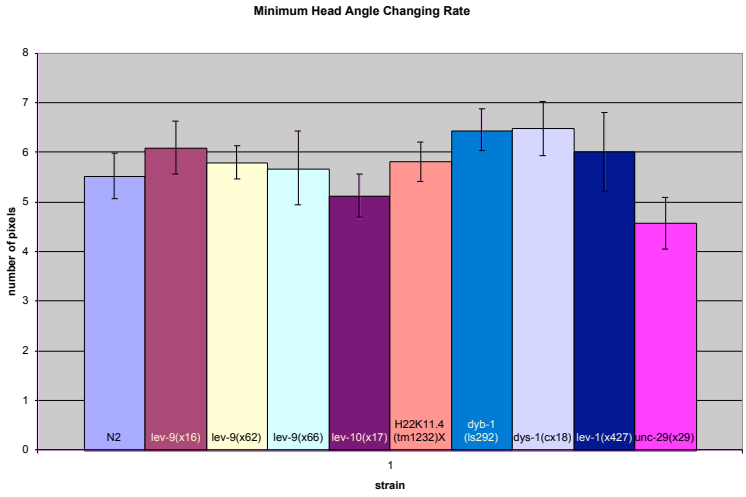

Figure 13 Mean values for the top three nodes in the classification tree. The mean value shown in the graphs was calculated first by taking the mean value of the specific feature throughout the entire five-minute recording, which was then averaged with all recordings for that strain.

The top graph contains mean values of ANCHRMAX, the middle graph contains mean values of MVHLFMAX, and the bottom graph contains mean values of HDANGMIN.

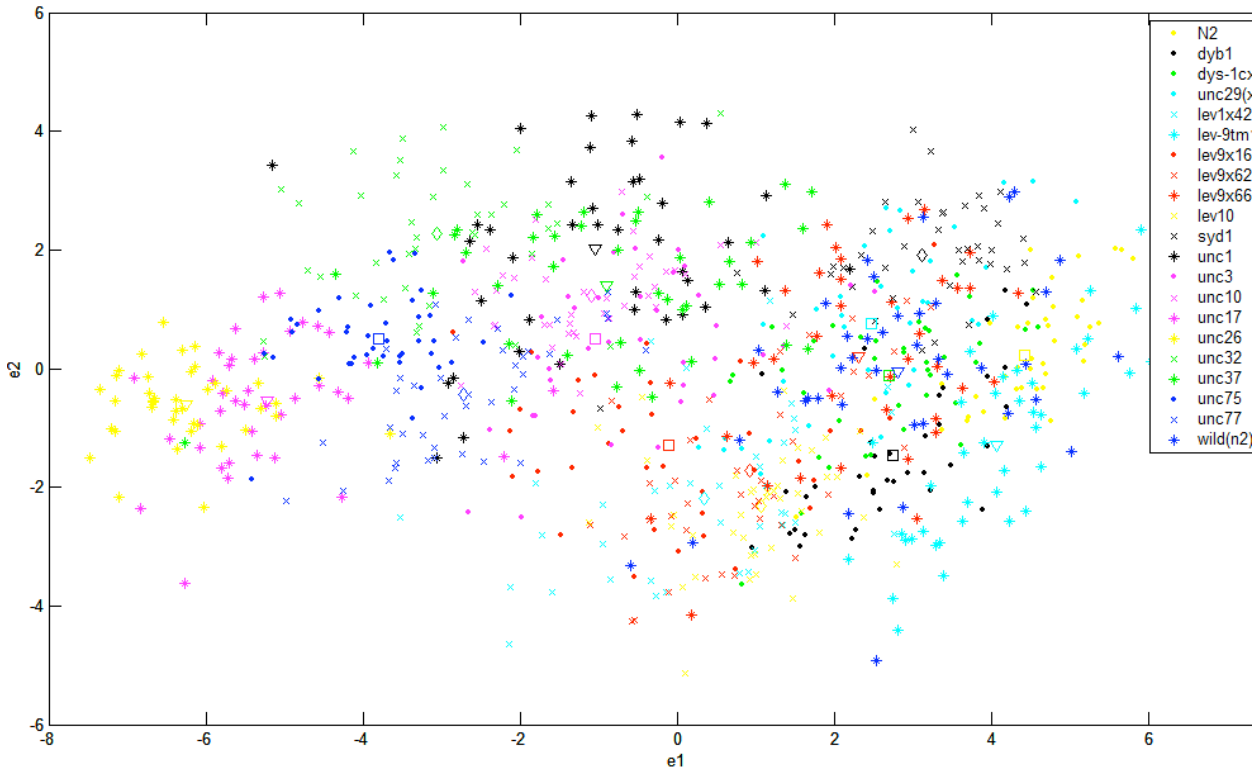

Figure 14 Combined cluster plot. Two dimensional cluster plot of *lev-9* mutants with severely uncoordinated worms. The severely uncoordinated worms clustered on the far left of the graph, while the position of *unc-29(x29)* was unchanged, leading to the conclusion that the data is unskewed and is being clustered correctly.

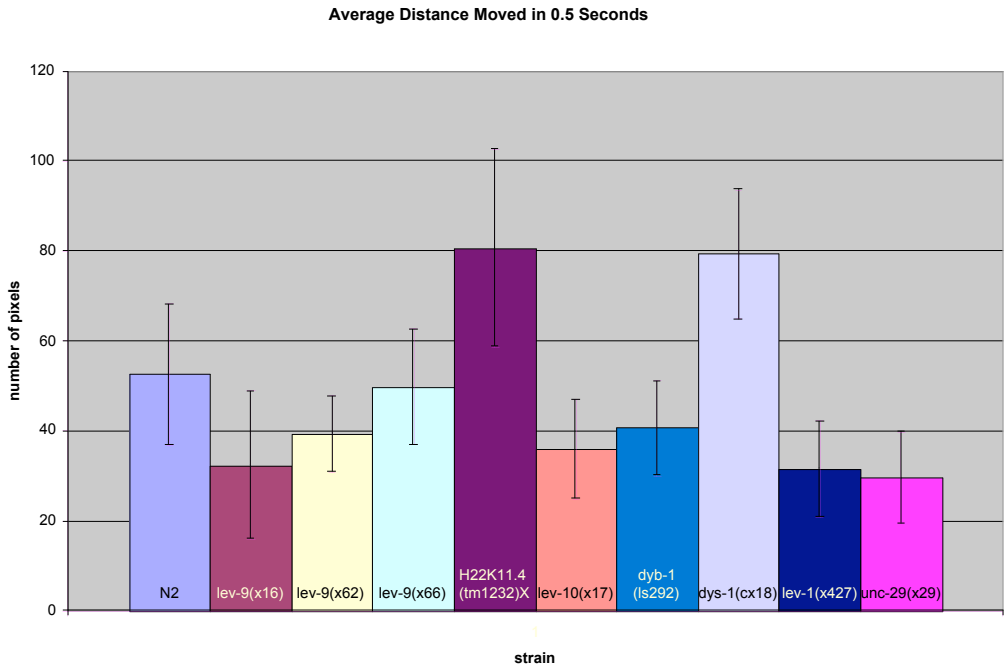

Figure 15 Average Distance Moved in 0.5 Seconds. Averages of the net distance moved in 0.5 seconds by each strain.

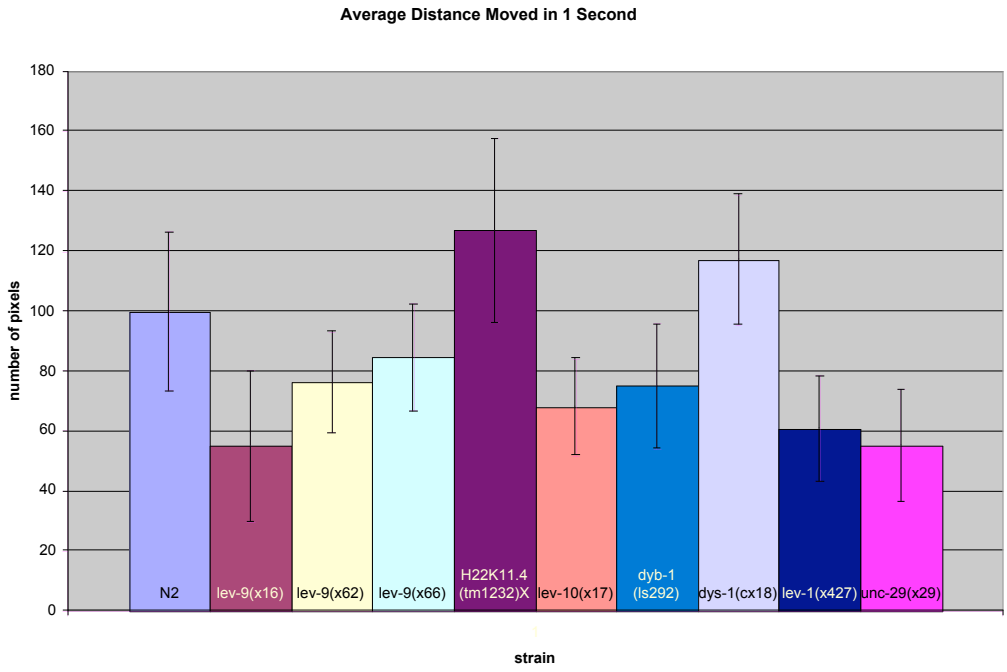

Figure 16 Average Distance Moved in 1 Second. Averages of the net distance moved in 1 second by each strain.

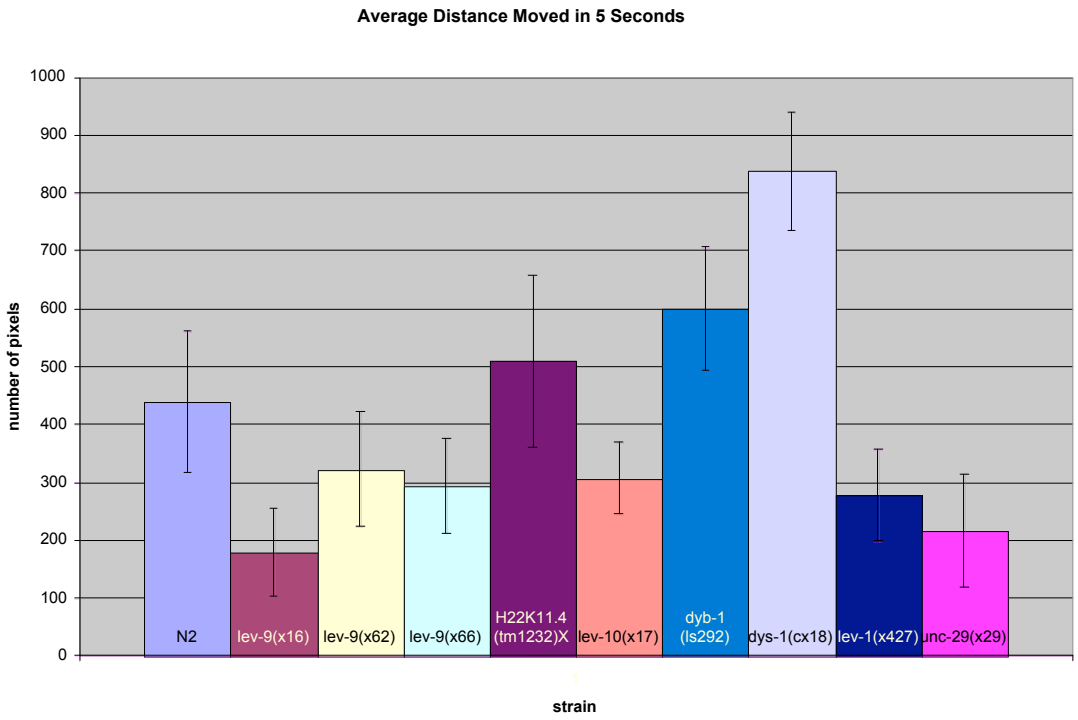

Figure 17 Average Distance Moved in 5 Seconds. Averages of the net distance moved in 5 seconds by each strain.

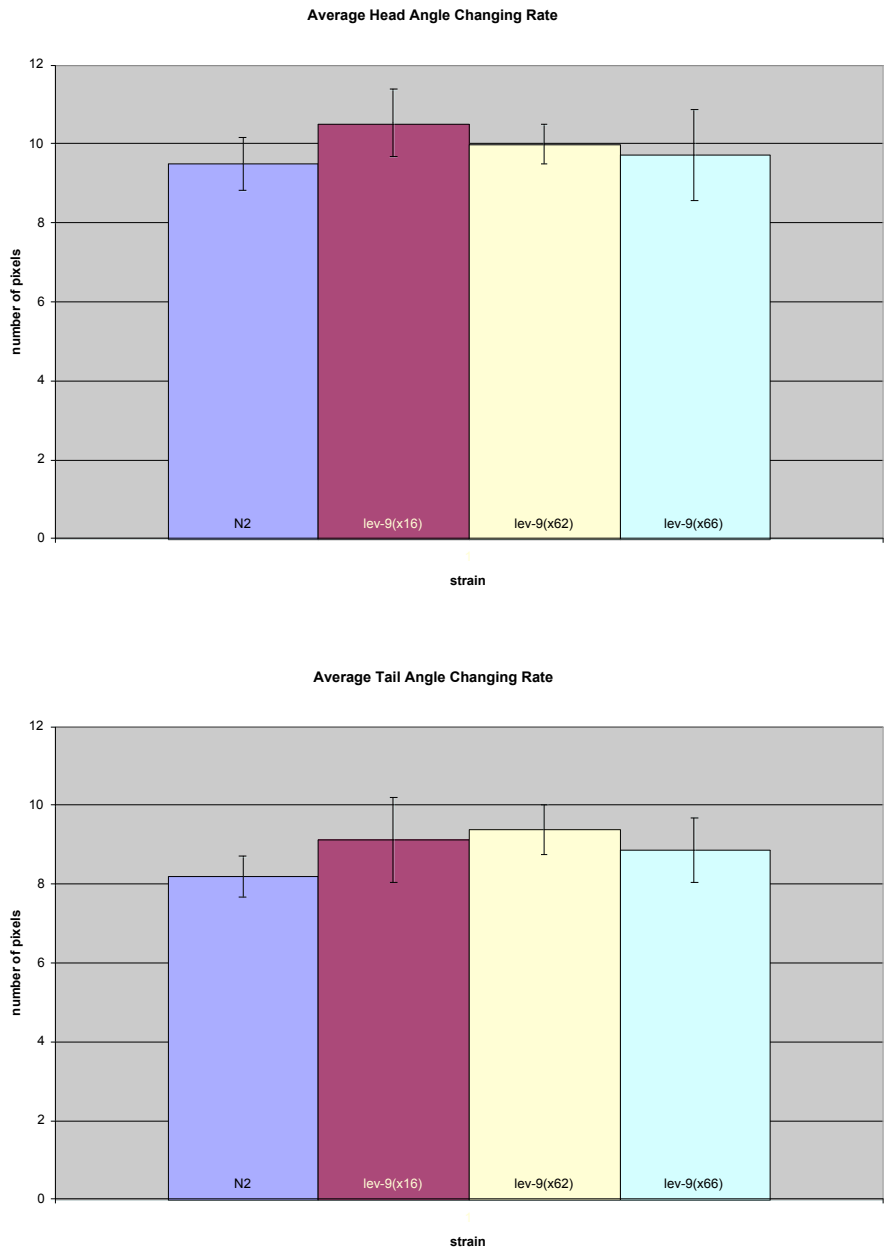

Figure 18. Average head and tail angle changing rates.

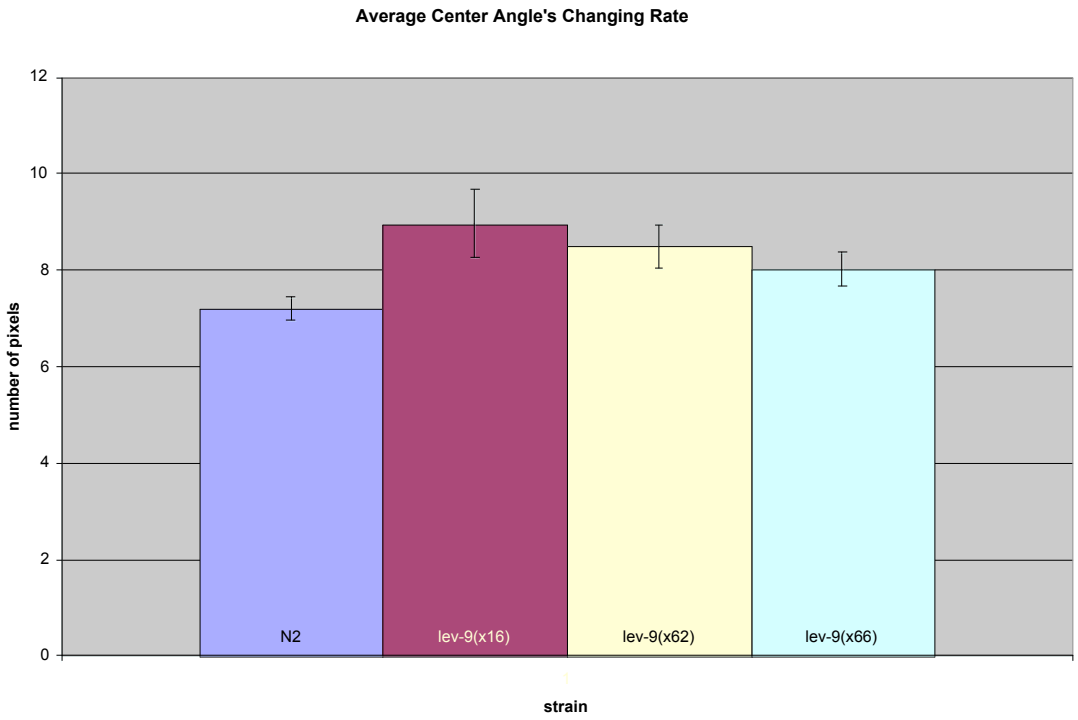

Figure 19 Average Center Angle Changing Rate.

CHAPTER IV: CONCLUSION

In this thesis, I have described two uses of an automated tracking and image analysis system. I participated in the development of an automatic egg-laying detection algorithm described in Chapter II which may be used for further study of *C. elegans* behavior. In addition, I used the automated tracking system to examine a mutant involved in nicotinic acetylcholine receptor function that was previously characterized as wild type, and found that this mutant displays subtle differences in behavior from wild type worms.

REFERENCES

J. Baek, P. Cosman, Z. Feng, J. Silver, and W. R. Schafer, "Using machine vision to analyze and classify C. elegans behavioral phenotypes quantitatively". J. Neurosci Meth **118**: 9 –21, 2002.

C. A. Bastiani, C.A., Gharib, S., Simon, M. I., Sternberg, P.W. "Caenorhabditis elegans Gq regulates egg-laying behavior via a PLCß-independent and serotonin-dependent signaling pathway and likely functions both in the nervous system and in muscle", Genetics **165**: 1805-1822, 2003.

C. Bessou, J. Giugia., C. Franks, L. Holden-Dye, and L. Ségalat, Mutations in the *Caenorhabditis elegans* dystrophin-like gene *dys-1* lead to hyperactivity and suggest a link with cholinergic transmission. Neurogenetics, **2**:61-72, 1998.

G. Borgefors, "Distance Transformations in Digital Images", Academic Press, 344-371, 1986.

L. Breiman, J. Friedman, R. Olshen, and C. Stone, Classification and Regression Trees, Wadsworth International Group, 1984.

S. Brenner, "The genetics of Caenorhabditis elegans". Genetics, **77**: 77-94. 1974.

A. Compton, S. Cooper, P. Hill, N. Yang, S. Froehner, and K.N. North, The Syntrophin-Dystrobrevin Subcomplex in Human Neuromuscular Disorders. Journal of Neuropathology and Experimental Neurobiology, **64**: 350-361, 2005.

J. M. Ervasti and K.P. Campbell, A role for the dystrophin-glycoprotein complex as a transmembrane linker between laminin and actin. *J. Cell Biol.* **122**: 809-823, 1993.

F. Escolano, M. Cazorla, D. Gallardo, and R. Rizo, "Deformable Templates for Tracking and Analysis of Intravascular Ultrasound Sequences", Proc. Of EMMCVPR'97, vol **1223**, 1997.

R. Fisker, J.M. Carstensen, M.F. Hansen, F. Bodeker, S. Morup, "Estimation of Nanoparticle Size Distributions by Image Analysis", Journal of Nanoparticle Research, **2(3)**: 267-277, 2000.

C. Gally, S. Elmer, J.E. Richmond, and J.-L. Bessereau, A transmembrane protein required for acetylcholine receptor clustering in *Caenorhabditis elegans*. Nature, **431**: 578-582, 2004.

J.-L. Galzi, F. Revah, A. Bessis and J.-P. Changeax, 1991 Functional architecture of the nicotinic acetylcholine receptor: from electric organ to brain. Ann. Rev. Pharmacology. **31:** 37-72.

K. Gieseler, C. Bessou, and L. Ségalat, Dystrobrevin- and dystrophin-like mutants display similar phenotypes in the nematode *Caenorhabditis elegans*. Neurogenetics, **2**:87-90, 1999.

W. Geng, P. Cosman, J-H Baek, C. Berry, and W.R. Schafer, "Quantitative Classification and Natural Clustering of *C. elegans* Behavioral Phenotypes". Genetics, **165**: 1117-1126, 2003.

W. Geng, P. Cosman, C. Berry, Z. Feng, and W.R. Schafer, "Automatic Tracking, Feature Extraction and Classification of *C. elegans* Phenotypes," *IEEE Transactions on Biomedical Engineering*. IEEE Transactions on Biomedical Engineering. Vol. **51**, No. 10: 1811-1820, 2004.

L.A. Hardaker., E. Singer, R. Kerr, G.T. Zhou, W.R.Schafer, "Serotonin Modulates Locomotory Behavior and Coordinates Egg-Laying and Movement in *Caenorhabditis* elegans", J. Neurobiol. **49**: 303-313, 2001.

A. Jain, Y. Zhong, and M-P Dubuisson-Jolly, "Deformable Template Models: A review", Signal Processing, **71**: 109-129, 1998.

A. Jain, Y. Zhong, and S. Lakshmanan, "Object Matching Using Deformable Templates", vol. **18**, no. 3: 267-277,1996.

R. Jain, K. Rangachar, and B. Schunck, *Machine Vision*, New York, McGraw-Hill, 1995.

J.A. Lewis, C.-H. Wu, J.H. Levine, and H. Berg, "Levamisole-resistant mutants of the nematode *Caenorhabditis elegans* appear to lack pharmacological acetylcholine receptors", Neuroscience, **5**: 967-989, 1980a.

J.A. Lewis, C.-H. Wu, H. Berg, and J.H. Levine, "The genetics of levamisole resistance in the nematode *Caenorhabditis elegans*", Genetics, **95**: 905-928, 1980b.

J.A. Lewis, J. S. Elmer, J. Skimming, S. McLafferty, J. Fleming, and T. McGee, Cholinergic receptor mutants of the nematode *Caenorhabditis elegans*. J. Neurosci. **7:** 3059-3071 1987.

T. McInerney and D. Terzopoulos, "Deformable Models in Medical Image Analysis: A Survey", Medical Image Analysis, **1(2)**: 91-108, 1996.

C.E. Metz, “Basic Principles of ROC Analysis”, Seminars in Nuclear Medicine, Vol. **VIII**, No. 4: 283-298, 1978.

J.E. Richmond and E. M. Jorgensen, One GABA and two acetylcholine receptors function at the *C. elegans* neuromuscular junction. Nat. Neurosci. **2:** 1–7, 1999.

H.M. Sadoulet-Puccio and L.M. Kunkel, Dystrophin and its isoforms. Brain Pathology **6**: 25-35, 1996.

M.Sonka, V. Hlavac, and R. Boyle, Image Processing, Analysis, and Machine Vision, Brooks/Cole Publishing Company, Second Edition, 1999.

C. Trent, N. Tsuing, and H. R. Horvitz, “Egg-laying defective mutants of the nematode Caenorhabditis elegans”, Genetics, **104**: 619-647, 1983.

L.E. Waggoner, L.A. Hardaker, S. Golik, and W.R. Schafer, “Effect of a neuropeptide gene on behavioral states in Caenorhabditis elegans egg-laying”. Genetics, **154**: 1181-1192, 2000.

L.E. Waggoner, G. T. Zhou, R. W. Schafer, W. R. Schafer, “Control of alternative behavioral states by serotonin in Caenorhabditis elegans”. Neuron **21**: 203-214, 1998.

D. Weinshenker, G. Garriga, and J.H. Thomas, “Genetic and pharmacological analysis of neurotransmitters controlling egg-laying in C. elegans”, J. Neurosci., **15**: 6975-6985, 1995.

J. White, E. Southgate, N. Thomson, and S. Brenner. “The structure of the Caenorhabditis elegans nervous system”. Philos. Trans. R. Soc. Lond. (Biol.) **314**: 1-340, 1986.

G.T. Zhou., W. R. Schafer, R. W. Schafer. “A three-state biological point process model and its parameter estimation”. IEEE Trans. Signal Process. **46**: 2698-2707, 1998.